Lund-mPh-16/01

Study of Proton Emission in Complex Nuclei

MASTER THESIS

Jonatan Adolfsson
Supervisors: Gillis Carlsson & Sven Åberg

March 10, 2016

LUND UNIVERSITY

Mathematical Physics
Lund University

Study of Proton Emission in Complex Nuclei

MASTER THESIS

Jonatan Adolfsson
Supervisors: Gillis Carlsson & Sven Åberg

March 10, 2016

Division of Mathematical Physics, Department of Physics, Lund University

Abstract

In a recent experiment, the partial half-life ($t_{1/2}$) of proton emission from the $I^\pi = 19/2^-$ state of ^{53}Co was accurately measured. A previous estimate is $t_{1/2} \sim 17\,\mathrm{s}$. The purpose of this thesis was to explain this decay and give a theoretical estimate for the dominating hindrance factors.

The angular momentum J in ^{53}Co is coupled to $J = 6$ for the neutrons, and $J = 7/2$ for the protons. All of this is transferred to the emitted proton during the decay. In a first approach, the neutron part was ignored and spherical symmetry assumed. Three different methods to describe this decay were tested and compared. These methods were validated by comparing computed reference half-lives to [1] and ^{53}Co half-life to results obtained from the computational code GAMOW [2]. Assuming this model, all of these methods were accurate, and a method based on probability flow was selected for further calculations. For ^{53}Co, the computed half-life was ~ 17 orders of magnitude too low in the first approach.

The method was improved by including the pairing interaction, giving an increase in $t_{1/2}$ by ~ 1.4. Next, nuclear deformation was included, and both proton and neutron overlaps were computed for different deformations β_2 of the mother nucleus, assuming axial symmetry. The proton overlap had only a minor effect on the decay time. The increase in angular momentum from $\ell = 3$ to $\ell = 9$ was estimated to add a factor of $\sim 3 \cdot 10^6$ to the decay time, and the $\ell = 9$ components of the proton wave function another factor of $\sim 4 \cdot 10^8 - 7 \cdot 10^9$. The remaining factor was conjectured to come from the neutron overlap, but in the model used, this was computed to be zero. This was expected to be resolved by extension to triaxial shapes.

Acknowledgements

I would like to thank my primary supervisor, Gillis Carlsson, for his continuous guidance and much appreciated help on this thesis. Without him, this would never had reached completion. Moreover, I would like to thank Sven Åberg for his time and advice during my work, Ingemar Ragnarsson for his estimate of the deformation of ^{53}Co, and Daniel Ward for his help with computing nuclear overlap. Finally, I would like to thank the rest of the Mathematical Physics Department for their support and for providing facilities for my work.

Contents

1 Introduction **1**
1.1 Aim and Structure of Thesis . . . 2

2 Spherical Symmetry **3**
2.1 Methods . . . 3
2.1.1 WKB Approximation . . . 3
2.1.2 Two-Potential Approach . . . 5
2.1.3 Probability Flow Approach . . . 6
2.1.4 Test of Energy Window for Different Methods . . . 9
2.1.5 Dependence on ℓ and Z for the Half-Life . . . 9
2.1.6 Spin-Orbit Interaction . . . 10
2.2 Results . . . 12
2.2.1 Results from Different Methods . . . 12
2.2.2 Test of Energy Window . . . 13
2.2.3 Dependence on ℓ and Z . . . 14
2.2.4 Spin-orbit Interaction . . . 15
2.3 Discussion . . . 15

3 The Nuclear Pairing Interaction **17**
3.1 Methods . . . 17
3.1.1 Basic Theory . . . 17
3.1.2 Practical Computations . . . 19
3.1.3 Effect on Half-Life Due to Pairing . . . 19
3.2 Results . . . 24
3.3 Discussion . . . 26

4 Deformation **27**
4.1 Methods . . . 27
4.1.1 Deformed Potential . . . 27
4.1.2 Calculation of Half-Life in the Deformed Case . . . 28
4.1.3 Nuclear Overlaps . . . 29
4.1.4 Connecting Overlaps to Radial Basis Functions . . . 31
4.2 Results . . . 32
4.3 Discussion . . . 34

5 Conclusions **37**

Chapter 1

Introduction

Nuclei on the neutron deficient side of the chart of nuclides have an excess of protons relative to the number of neutrons, and therefore decay into more neutron-rich nuclei. Usually, this occurs through electron capture or β^+ decay, i.e., one proton decays to a neutron. For some nuclei far from the β-stability line, however, another decay branch is possible: proton emission. This means simply that the neutron deficient nucleus emits one of its protons, i.e., we have the reaction

$$ {}^{A}_{Z}X_N \rightarrow {}^{A-1}_{Z-1}Y_N + p, \tag{1.1} $$

where X is the mother nucleus, Y is the daughter nucleus, and p is a proton. This is quite similar to α decay observed in heavy nuclei.

In order for proton emission to occur, the reaction Eq. 1.1 must be energetically possible. This does not mean that the emitted proton is necessarily unbound; instead it may be trapped as a quasi-bound state within the Coulomb barrier, which is present since protons are charged (as opposed to neutrons). In a crude picture, the proton may then tunnel through the barrier, as described in Figure 1.1. This is the basic mechanism of proton emission. In order to describe the process more accurately, though, one has to take into account structural changes of the nucleus as well, and a more sophisticated model than considering the proton as a free particle within a nucleus might be required.

The first nucleus in which proton emission was observed is an excited state of ^{53}Co, at 3197 keV [3]. Although the proton emission branch was discovered already in 1970 [4], the branching ratio for this decay was not successfully measured until 2015, in a not yet published measurement by a group led by Luis Sarmiento at Lund University. The reason for this is that the other decay branch, which is a β^+-decay, is very similar in both decay time and energy to the β^+-decay of the ground state of ^{53}Co, and these decays are thus very difficult to separate [5].

If the branching ratio b for a certain decay branch is known, the partial decay time may be determined as

$$ t_{1/2}^{part} = \frac{t_{1/2}}{b}, \tag{1.2} $$

where $t_{1/2}$ is the observed half-life, and $t_{1/2}^{part}$ is the partial half-life in the interesting decay channel. If $t_{1/2}^{part}$ is known, this may be used to determine theoretical model parameters and eventually increase the understanding of this decay mode. To start out, however, one needs to set a theoretical framework and obtain a basic understanding for the decay. Since the mother nucleus is in a state with $I^\pi = 19/2^-$, and the daughter nucleus is in a state with $I^\pi = 0^+$ (the remaining angular momentum is transferred to the proton), the proton emission decay of ^{53}Co involves large structural changes in the nucleus and large angular momentum transfers.

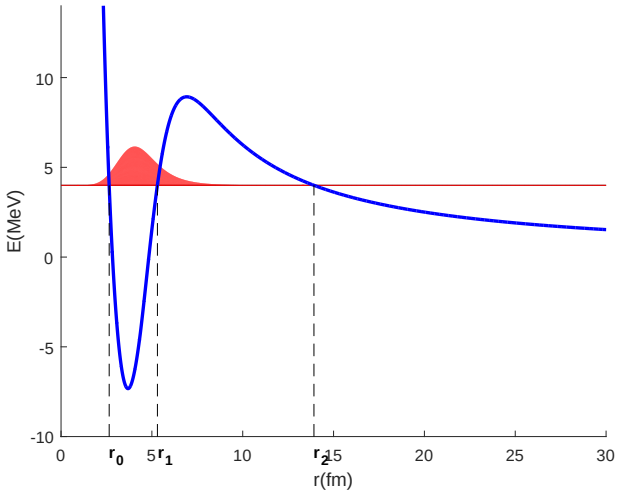

Figure 1.1 – Basic principle behind proton emission. One of the protons, represented by the red wave package is in an orbital where the energy is greater than the free-particle energy, and thus exists as a quasibound state within the nucleus. The points r_1 and r_2 are known as the inner and outer turning points, and define the endpoints of the classically forbidden region. The proton may eventually tunnel out of the nuclear Coulomb barrier (blue), which happens if it is observed at a distance from the core $r > r_2$. The point r_0 marks the endpoint of the classically allowed region for the bound state.

Therefore, this is quite a complex decay. As a consequence, the decay time is significantly longer than in a crude model not involving structural changes.

1.1 Aim and Structure of Thesis

The aim of this thesis is to explain the observed decay time in the proton branch of ^{53}Co. This is done by starting out from a simple decay model, and then stepwise increasing the complexity until an adequate description of the decay mechanism is established. In this way, the main hindrance factors are determined. If successful, these methods may be used to study other proton emissions from a theoretical point of view.

This thesis is structured as follows. In the first part, three different methods are used to study proton emission in a spherically symmetric model, not including structural changes. In the second part, structural changes of the protons are added by applying the nuclear pairing interaction to the original model. In the final part, the study is expanded to deformed nuclei, where a change in deformation occurs. In this part, the effects of structural changes are also studied for the neutrons.

To get a measure for the quality of each model, the results were compared to the previous estimate (before the new measurement) of the branching ratio for proton emission of $b \sim 1.5\%$, which using Eq. 1.2 and the observed half-life of 247(12) ms [3] gives a partial half-life of ~ 17 s in the proton emission branch.

The computations used for this thesis were carried out by either using MATLAB (mostly used when working in spherical symmetry) or the Fortran programming language (mostly used for deformed systems). All figures in this report are generated using MATLAB.

Chapter 2

Study of Proton Emission In Spherical Symmetry and not Involving Structural Changes

In this part, three different methods assuming spherical symmetry and not involving structural changes are studied. These are:

- The *WKB Approximation*, which is a semi-classical model where the proton is treated as a free particle within the nucleus (cf. Figure 1.1), and the probability of tunnelling through the proton barrier is calculated.
- The *Two-Potential Approach* (TPA), where the proton is again treated as a free particle. Here, the part of the potential outside the potential maximum in Figure 1.1 is treated as a perturbation to the rest of the potential, and the resulting parts of the wave function are matched to get a neat expression for the half-life.
- The *Probability Flow Approach* (PFA), where the total probability flow was computed by using the proton wave function, which gives a measure of the decay probability.

These methods were applied to ^{53}Co and were validated by testing each of the models on other – from a theoretical point of view – more well-known examples of proton emission. The tests were complemented by using an established computational code for computing energies and decay widths of nuclear states. Moreover, the energy window and dependence on charge and angular momentum were tested for each of the methods.

2.1 Methods

2.1.1 WKB Approximation

The WKB (Wentzel-Kramers-Brillouin) approximation is a semi-classical model for approximating half-lives for proton emission. In this simple model, the proton and the daughter nucleus are treated as separate objects, and the proton is considered to tunnel through the potential barrier. This model is good as a first approach, in order to get an intuitive understanding for the mechanisms behind proton emission.

The decay width Γ is generally defined as

$$\Gamma = \frac{\hbar}{t_{1/2}} \ln 2, \tag{2.1}$$

where $\hbar$ is Planck's constant. The partial decay width for proton emission (henceforth, I will not bother about full decay widths, and the variable $t_{1/2}$ will refer to the partial decay width in the proton channel) in the WKB approximation (this is simply the tunnelling probability) is [1]

$$\Gamma = \mathcal{N}\frac{\hbar^2}{4\mu}\exp\left(-2\int_{r_1}^{r_2}|k(r)|dr\right), \tag{2.2}$$

where μ is the reduced mass of the proton, $k(r)$ is the classical momentum, defined as

$$k(r) = \frac{1}{\hbar}\sqrt{2\mu(E - V_{eff}(r))}, \tag{2.3}$$

where $E = Q_p$ is the decay energy, V_{eff} is the effective nuclear potential, r_1 and r_2 are the inner and outer turning points, respectively, which are defined in Figure 1.1, and $\mathcal{N}$ is a normalisation constant. The reduced mass is in this case

$$\mu = m_p \cdot \frac{m_D}{m_D + m_p}, \tag{2.4}$$

where m_p is the proton mass and m_D is the mass of the daughter nucleus. The normalisation constant was calculated according to [1], as

$$\mathcal{N}^{-1} = \frac{1}{2}\int_{r_0}^{r_1}\frac{dr}{k(r)}, \tag{2.5}$$

where r_0 and r_1 are the endpoints of the classically allowed region for the bound state of the proton (cf. Figure 1.1). The effective potential is constructed by adding the Woods-Saxon potential generated by the nucleus to the Coulomb potential and a part depending on the angular momentum ℓ. The result if neglecting spin-orbit interaction is [6, pp. 54 & 64]

$$V_{eff}(r) = -\frac{V_0}{1 + \exp((r - R)/a)} + V_C(r) + V_\ell(r), \tag{2.6}$$

where

$$V_C(r) = \begin{cases} -\dfrac{Ze^2}{4\pi\epsilon_0 R}\left(\dfrac{r^2}{2R^2} - \dfrac{3}{2}\right), & r < R \\ \dfrac{Ze^2}{4\pi\epsilon_0 r}, & r > R, \end{cases} \tag{2.7}$$

and

$$V_\ell(r) = \frac{\hbar^2\ell(\ell+1)}{2\mu r^2}, \tag{2.8}$$

where $R = r_0 A^{1/3}$, A is the mass number and Z is the charge of the daughter nucleus (the proton does not feel the potential of itself), and V_0, a and r_0 are model parameters. Analogous to [1], I have fixed $r_0 = 1.17\,\text{fm}$ and $a = 0.75\,\text{fm}$, and I use V_0 as a free parameter.

In order to get a potential where the lowest positive proton energy E agrees with the measured value Q_p, the time-independent Schrödinger equation was solved to obtain the energies and wave functions (the latter are used in Section 2.1.2). This was done by replacing V_{eff} with $\tilde{V}$, where

$$\tilde{V} = \begin{cases} V_{eff}, & r < r_{max} \\ V_{max}, & r > r_{max}, \end{cases} \tag{2.9}$$

where (r_{max}, V_{max}) is the position of the maximum of the potential barrier. This was done to get a bound state also for quasi-bound states where $E > 0$. This is expected to be a

reasonable approximation, since the amplitude of the wave function is expected to be very low at $r > r_{max}$. Then the Schrödinger equation becomes

$$\left(-\frac{\hbar^2}{2\mu r}\frac{\partial^2}{\partial r^2}r + \tilde{V}\right)\psi(r) = E\psi(r). \tag{2.10}$$

This was solved numerically, by discretising the Hamilton operator $H = T + \tilde{V}$ at grid points r_i, placed at fixed spacings Δr, according to

$$H(r_i)\psi(r_i) \approx \frac{\hbar^2}{2\mu}\frac{\left(1+\frac{\Delta r}{r_i}\right)\psi(r_{i+1}) - 2\psi(r_i) + \left(1-\frac{\Delta r}{r_i}\right)\psi(r_{i-1})}{\Delta r^2} + \tilde{V}(r_i)\psi(r_i), \tag{2.11}$$

and solving the corresponding eigenvalue problem. The resulting eigenvectors $\psi(r)$ were normalised (for later use) to satisfy

$$\int_0^\infty |\psi(r)|^2 r^2 dr = 1, \tag{2.12}$$

where ∞ was replaced by the upper end of the vector r in the numerical case. The lowest energy eigenvalue E_1 was matched to Q_p by minimising $|E_1 - Q_p|$ iteratively, using 18 iterations of Golden Section line search with V_0 as a free parameter. As starting values the range $V_0 \in [30, 70]$ MeV was used. The final value was obtained as the mean of the two endpoints of the final interval.

For ^{53}Co, the grid used was $r \in [0.01, 45]$ fm, with $\Delta r = 5 \cdot 10^{-3}$ fm. Here, r was chosen to start at a non-zero value to avoid complications with infinities in Eq. 2.11. For this nucleus, the proton exists in an $f_{7/2}$ subshell and thus $\ell = 3$. Since this model does not take into account structural changes, which would give the emitted proton an angular momentum of $\ell = 9$ (setting $\ell = 9$ would not create a bound state in this model, so this is not an option), it was for simplicity assumed that $\ell = 3$ for the outgoing proton. This was used to evaluate Eq. 2.6. In reality, the Q-value would be negative if not taking into account structural changes of the neutrons (derived from [3]), and instead the observed value of $Q_p = 1.53\,\text{MeV}$ was used, along with the measured value $m_D = 51.93\,\text{u}$ [3]. Using the resulting potential V_{eff} and corresponding energy E_1, an approximative value of Γ was obtained by using Eq. 2.2. By using Eq. 2.1, the half-life was computed.

As a validation of the method, half-lives were computed for the isotopes ^{105}Sb, ^{113}Cs, ^{147}Tm, ^{157}Ta and ^{165}Ir, which have previously been studied in [1]. This was done using the same parameters as in the original article, which are given in Table II in [1], and estimating the nuclear mass as $1\,\text{u} \cdot A$, where A is the mass number. For these isotopes, the grid $r \in [0.01, 165]$ fm, with $\Delta r = 0.01\,\text{fm}$, was used.

2.1.2 Two-Potential Approach

This method (henceforth TPA) is described in detail in [1]. It is another method which does not take into account changes in structure.

Formally, the potential V_{eff} defined by Eq. 2.6 may be split into $V_{eff}(r) = \tilde{V}(r) + W(r)$, where $\tilde{V}$ is defined in Eq. 2.9, and

$$W(r) = \begin{cases} 0, r \leq r_{max} \\ V(r) - V_{max}, r > r_{max}. \end{cases} \tag{2.13}$$

Here, one may introduce $\tilde{W}(r) = W(r) + V_{max}$ and solve the Schrödinger equation using this potential, which is now treated as a perturbation to $\tilde{V}(r)$ (the reason for adjusting the

zero-level by adding V_{max} is to find a solution which vanishes as $r \to \infty$). Defining the regular eigenfunction for this problem as $\chi(r)$, the decay width may then be approximated as [1]

$$\Gamma = \frac{\hbar^2}{\mu k} \left| \psi(r_{max})(\alpha\chi(r_{max}) + \chi'(r_{max})) \right|^2, \tag{2.14}$$

where $k = \sqrt{2\mu E}/\hbar$ in this section, $\alpha = \sqrt{2\mu(V_{max} - E)}/\hbar$, and E and $\psi(r)$ are the solution to Eq. 2.10, which is lowest in energy E. Since the proton is mainly affected by the Coulomb potential at $r \geq r_{max}$, $\chi(r)$ may be replaced by – according to [1] – the regular Coulomb wave function $F_\ell(\eta, \rho)$, where $\rho = kr$,

$$\eta = \frac{\mu e^2 (Z-1)}{4\pi\epsilon_0 \hbar^2 k}, \tag{2.15}$$

and ℓ is the orbital angular momentum. This approach is the one used in this section.

The regular Coulomb wave function may be written as [7, p. 538]

$$F_\ell(\eta, \rho) = \frac{2^\ell \exp(-\pi\eta/2)|\Gamma(\ell + 1 - i\eta)|}{\Gamma(2\ell + 2)} \rho^{\ell+1} \exp(-i\rho) M(\ell + 1 - i\eta, 2\ell + 2, 2i\rho), \tag{2.16}$$

where $\Gamma(z)$ is the Γ function, and [7, p. 504]

$$M(a, b, z) = \sum_{k=0}^{\infty} \frac{(a)_k z^k}{(b)_k k!} \tag{2.17}$$

is Kummer's function, where

$$(a)_k = \prod_{i=0}^{k-1} (a + k) \tag{2.18}$$

for $k > 0$, and $(a)_0 = 1$, and analogous for $(b)_k$. Numerically, Kummer's function was calculated by including the first 80 terms in Eq. 2.17 (this turned out to be enough for convergence in the relevant region). The Γ function was computed as $\Gamma(z) = (z-1)!$ for integer z. For non-integer or complex z, $\Gamma(z)$ was approximated by using Stirling's formula [7, p. 257],

$$\Gamma(z) \sim \exp(-z) z^{z-\frac{1}{2}} \sqrt{2\pi} \left(1 + \frac{1}{12z} + \frac{1}{288z^2} - \frac{139}{51840z^3} - \frac{571}{2488320z^4} \right). \tag{2.19}$$

The derivative, $\frac{\partial}{\partial r} F_\ell(\eta, \rho)$ was computed as a simple difference quotient,

$$\frac{\partial}{\partial r} F_\ell(\eta, kr_i) \approx \frac{F_\ell(\eta, kr_{i+1}) - F_\ell(\eta, kr_{i-1})}{2\Delta r}. \tag{2.20}$$

By inserting the obtained values for $F_\ell(\eta, kr_{max})$ and $F'_\ell(\eta, kr_{max})$ into Eq. 2.14, decay widths and corresponding half-lives were computed for ^{53}Co, as well as the same reference isotopes as in Section 2.1.1.

2.1.3 Probability Flow Approach

Original Method

This method (henceforth PFA) is yet another approach for measuring the penetrability for the proton during proton emission, i.e., the decay time without considering structure changes. In fact, this method has mainly been used for computing α decay times, but this time – perhaps for the first time ever – it was tested for proton emission instead.

The basic principle for PFA is that the decay width may be interpreted as a measure of the probability flow out of a spherical surface (in fact, any spherical surface) surrounding the core. The details are derived in [8]. Following some simplifications by Gillis Carlsson, the decay rate may be obtained as

$$\lambda = j(r_0), \tag{2.21}$$

where

$$j(r) = r^2 \left(\psi(r)\psi'(r)^* - \psi(r)^*\psi'(r)\right) \frac{i\hbar}{2\mu} \tag{2.22}$$

is the radial probability flow through a surface, and r_0 is an arbitrary distance from the origin. For large r_0, the result is independent of the particular choice of r_0. For outgoing waves, as is the case for proton emission, and assuming k is real, Eq. 2.22 may be simplified as

$$j(r) = r^2|\psi(r)|^2 \cdot v, \tag{2.23}$$

where $v = \sqrt{2E/\mu}$ is the non-relativistic speed of the proton. For large r_0, $C \equiv r_0^2|\psi(r_0)|^2$ is essentially constant, i.e.,

$$j(r_0) = C \cdot v. \tag{2.24}$$

To find C, one may match an internal solution, obtained by solving the Schrödinger equation close to the nucleus, as done in Section 2.1.1, with an outgoing solution, which in the presence of a Coulomb potential is

$$\psi_a(r) = \frac{1}{r}(G_\ell(\eta, kr) + iF_\ell(\eta, kr)). \tag{2.25}$$

Here F_ℓ is the regular Coulomb wave function and G_ℓ is the irregular Coulomb wave function[1]. This is required since the internal solution is only a good approximation of the true wave function at small values of r. Therefore,

$$\psi(r) = \frac{\psi(r_m)}{\psi_a(r_m)}\psi_a(r), \tag{2.26}$$

for large r, where r_m is a matching point. By inserting Eq. 2.26 into Eq. 2.23 and Eq. 2.21, and taking the limit $r \to \infty$, one obtains

$$\lambda = \lim_{r\to\infty} r^2 \left|\frac{\psi(r_m)}{\psi_a(r_m)}\psi_a(r)\right|^2 \cdot v = \left|\frac{\psi(r_m)}{\psi_a(r_m)}\right|^2 \cdot v. \tag{2.27}$$

Here, the last expression is a consequence of the asymptotic behaviour [7, p. 542]

$$G_\ell(\eta, \rho) + iF_\ell(\eta, \rho) \to \exp(i(\rho - \eta \ln 2\rho - \frac{\ell\pi}{2} + \sigma_\ell)), \tag{2.28}$$

where σ_l is a constant, as $\rho \to \infty$. Therefore, $C = |\psi(r_m)/\psi_a(r_m)|^2$.

The regular Coulomb wave function was calculated as in Section 2.1.2. The irregular part, G_ℓ, was calculated using the relation

$$G_\ell(\eta, \rho) = \frac{\Gamma(\ell + 1 - i\eta)}{|\Gamma(\ell + 1 - i\eta)|} \exp(\pi\eta/2) i^\ell W_{i\eta,\ell+1/2}(2i\rho) + iF_\ell(\eta, \rho), \tag{2.29}$$

where $W_{a,b}(z)$ is the Whittaker function, which was evaluated numerically using the built-in function in MATLAB. Unfortunately, this is a very slow routine, and therefore G_ℓ was only evaluated at a few points.

[1] The regular and irregular Coulomb wave functions are two special linearly independent solution to the Schrödinger equation in the presence of a Coulomb potential, see e.g. [7, p. 538].

The matching points r_m, were selected as 30 equidistant points on an interval somewhere between the inner and outer turning points of the potential barrier (cf. Figure 1.1). These matching points were used, since both the internal and Coulomb wave functions were expected to be good approximations for the true wave function here. The turning points were obtained from the WKB calculations. In order to accurately evaluate the wave functions in this interval, these were re-evaluated by solving Eq. 2.10 and replacing $\tilde{V}$ by V_{eff}, and again optimising the Woods-Saxon potential depth V_0 using Golden Section search. As an outer boundary condition, a Dirichlet condition was placed at $r = r_M$, where

$$r_M = \max\left(r_2 + \frac{1}{2}(r_2 - r_1), 2r_{max}\right), \tag{2.30}$$

where r_1, r_2 and r_{max} are defined as in Section 2.1.1. The reason for not going further out is that the Dirichlet condition creates a second potential well outside the potential barrier, which is a false state. Therefore, the state with lowest energy might not be a resonant state of the nucleus. Therefore, the process of solving the Schrödinger equation was iterated over increasing energy eigenvalues, until a state for which the maximum of $|\psi(r)|$ was located within the barrier. For large r_M, such a state was difficult to find. The reason for requiring $r_M \geq 2r_{max}$, is that when the barrier is thin, $V(r_M)$ might otherwise be so large that it is not reasonable to put a Dirichlet boundary condition at this position.

Moreover, Golden Section search requires that the function $|E - Q|$ is unimodal, which is not the case. On the other hand, it is expected to be unimodal in a small interval around the correct barrier height V_0. Therefore, for the PFA method, Golden Section search was carried out on the interval $V_0 \in [V_0^0 - \delta, V_0^0 + \delta]$, where V_0^0 is the value of V_0 obtained from the WKB method, $\delta = 30\,\text{keV}$ was used for ^{53}Co, and $\delta = 10\,\text{keV}$ was used for ^{105}Sb, ^{113}Cs, ^{147}Tm, ^{157}Ta and ^{165}Ir.

It turned out that the obtained values of λ were reasonably constant on the interval $r \in [r_1 + 0.15(r_2 - r_1), r_1 + 0.50(r_2 - r_1)]$ for all isotopes. Therefore, $\lambda \equiv \overline{\lambda}$ was taken as the average of all 30 evaluations on this interval. Using this λ, the half-life was computed as

$$\overline{t_{1/2}} = \frac{\ln 2}{\overline{\lambda}}. \tag{2.31}$$

Improvement of PFA Using an Iterative Method

Although it turned out the results obtained from PFA agree well with WKB and TPA, one may yet want to improve this method for increased accuracy. In particular, the wave number $k = \sqrt{2\mu E}$ enters the Coulomb wave functions in Eq. 2.25. Moreover, the simplification Eq. 2.23 assumes that k is real. However, a decaying state is unbound, and thus has complex energy

$$E = E_0 - \frac{i\Gamma}{2} = E_0 - \frac{i\hbar\lambda}{2}, \tag{2.32}$$

where E_0 is the real part of the energy, coinciding with the Q-value.

To improve the solution obtained earlier in Section 2.1.3, Eq. 2.22 was thus iterated until convergence, where $\psi(r)$ is given in Eq. 2.26. With this wave function, one obtains

$$\psi'(r) = \frac{\psi(r_m)}{\psi_a(r_m)}\left(\frac{1}{r}(G'_\ell(\eta, kr) + iF'_\ell(\eta, kr)) - \frac{1}{r^2}(G_\ell(\eta, kr) + iF_\ell(\eta, kr))\right), \tag{2.33}$$

where $'$ denotes derivative with respect to r. Again, this was evaluated using a simple difference quotient. Inserting Eq. 2.33 into Eq. 2.22, one obtains after simplification

$$\lambda = C^2(O(r_0)O'(r_0)^* - O(r_0)^*O'(r_0))\frac{i\hbar}{2\mu}, \tag{2.34}$$

where $C^2 = |\psi(r_m)/\psi_a(r_m)|^2$,

$$O(r) = G_\ell(\eta, kr) + iF_\ell(\eta, kr), \tag{2.35}$$

and r_0 is an arbitrary choice of $r > r_2$, where r_2 is the outer turning point.

After each iteration, a new value of k was obtained as one solution to $k = \sqrt{2\mu E}$, where E is given by Eq. 2.32. Since the different values of λ computed at different grid points were expected to be almost the same, the average value $\overline{\lambda}$ was used in each iteration when evaluating Eq. 2.32.

During the first iteration, λ was obtained using Eq. 2.27. For further iterations, Eq. 2.34 was used instead. To avoid divergence when evaluating the sum Eq. 2.17, the fairly small value $r_0 = 1.5r_2$ was used. The iterations were repeated until the relative difference between two consecutive values of λ was $< 10^{-4}$. At high energies, there was a problem with convergence of Eq. 2.32. For this reason, the approximate relation

$$E = E_0 - 0.45i\hbar\lambda \tag{2.36}$$

was used instead when testing the method. This was for simplicity done for all energies.

2.1.4 Test of Energy Window for Different Methods

The results from the methods described in Sections 2.1.1, 2.1.2 and 2.1.3 seem to agree very well for all computed nuclei, which will be seen in Section 2.1. Yet, one may ask for which energy window each method is valid. In order to test this, the computational code GAMOW, ref. [2], was used to compute the imaginary part of the energy using outgoing boundary conditions. The code was slightly modified to print out the results at higher precision. Moreover, certain flags were used to use double precision during computations, as opposed to standard float position. The computation mode used, fixed the real part of the energy and varied the imaginary part and potential to find a single-node wave function with this energy.

For a resonant state, the decay width may be written as

$$\Gamma = -2\mathrm{Im}\, E, \tag{2.37}$$

and therefore accurate values of Γ were obtained using GAMOW. Corresponding values of $t_{1/2}$ were obtained using Eq. 2.1.

A comparison between the above mentioned methods was done by fixing all parameters for ^{53}Co at energies $Q = 1, 2, 3, 4, 5, 6, 7, 8, 9$, and 9.8 MeV and computing corresponding $t_{1/2}$ using each of the methods, as well as GAMOW. For PFA, $\delta = 1\,\mathrm{MeV}$ was used for $Q \leq 7\,\mathrm{MeV}$, $\delta = 2\,\mathrm{MeV}$ for $Q = 8\,\mathrm{MeV}$, and $\delta = 5\,\mathrm{MeV}$ for $Q \geq 9\,\mathrm{MeV}$. Moreover, both the original and the improved versions of PFA were tested. The value $Q = 9.8\,\mathrm{MeV}$ corresponds to a state at the top of the barrier.

As a further check, the half-life for the actual energy, $Q = 1.53\,\mathrm{MeV}$, was computed using GAMOW.

As a final check, the computation mode in GAMOW was changed to compute energies for fixed potentials, which were obtained from the WKB computations. This was done for all energies used previously in this section, including the Q-value of 1.53 MeV, to see how much each energy changes. This gave a measure of the stability of the previous results.

2.1.5 Dependence on ℓ and Z for the Half-Life

To get an intuitive understanding for the circumstances which favour proton emission, one may further check the dependence on ℓ and Z to the half-life. The ℓ dependence was tested

by varying ℓ and fixing $Q = 1.53\,\text{MeV}$ for ^{53}Co. As before, this was done by varying the potential depth V_0. It turned out that it was possible to find a bound state at $E = 1.53\,\text{MeV}$ for $V_0 \in [30, 50]\,\text{MeV}$ for $1 \leq \ell \leq 3$. The method selected for computing the half-lives was PFA.

In order to check whether the half-life depends significantly on A, A was varied between 47 and 59, while fixing $Z = 27$ and $\ell = 3$, and the corresponding half-lives were computed using PFA.

Although the results (see Section 2.2.3) indicate quite a weak dependence on neutron number, one still wants to preserve some properties of ^{53}Co while varying Z, in order to minimise the small dependence on A to the half-life, which after all is present. For this isotope it means that nuclei not very far from the line of β-stability (for cobalt, this is defined by ^{59}Co), but on the neutron deficient side, should be compared. For spherical nuclei, the condition for β-stability for fixed A is [6, p. 22]

$$N - Z = \left(\frac{3}{10} \cdot \frac{e^2}{4\pi\epsilon_0 R_C} A - \frac{1}{2}(M_n - M_H)c^2 \right) / \left(\frac{a_{sym}}{A} + \frac{3}{10} \cdot \frac{e^2}{4\pi\epsilon_0 R_C} \right), \tag{2.38}$$

where N is the neutron number, R_C is the Coulomb radius, M_n is the neutron mass, M_H is the mass of ^{1}H, and a_{sym} is the nuclear symmetry parameter in the liquid drop model. Reasonable estimates for the model parameters are $R_C = 1.2249 \cdot A^{1/3}\,\text{fm}$, and $a_{sym} = 55.24\,\text{MeV}$ [6, pp. 16-17].

I am, however, interested in the condition for β-stability for fixed Z. Since nuclei with $Z \in [17, 97]$ along the line of β-stability satisfy $2Z \leq A \leq 2.5Z$, it holds that $1.26Z^{1/3} \leq A^{1/3} \leq 1.36Z^{1/3}$. Therefore, the estimate $A^{1/3} \approx 1.31Z^{1/3}$ was made, and R_C could be treated as a constant for fixed Z. By substituting A by $N + Z$, Eq. 2.38 was solved for N, giving the result

$$\begin{aligned} N_{\beta-stable}(Z) &\simeq \frac{\left(55.24\,\text{MeV} - \frac{1}{2}(M_n - M_H)c^2\right) Z + \frac{3}{5} \cdot \frac{e^2}{4\pi\epsilon_0 \cdot 1.605 Z^{1/3}\,\text{fm}} Z^2}{55.24\,\text{MeV} + \frac{1}{2}(M_n - M_H)c^2 - \frac{3}{5} \cdot \frac{e^2}{4\pi\epsilon_0 \cdot 1.605 Z^{1/3}\,\text{fm}} Z} \\ &= \frac{54.85Z + 0.54Z^{5/3}}{55.63 - 0.54Z^{2/3}}. \end{aligned} \tag{2.39}$$

In order to test nuclei somewhat on the neutron deficient side, and to include ^{53}Co, the number of neutrons was decreased by $6Z/27 = 2Z/9$, resulting in

$$A(Z) = Z + N_{\beta-stable}(Z) - \frac{6Z}{27}. \tag{2.40}$$

Half-lives for $Z = 17, 27, \ldots, 97$ were computed using PFA for A given by Eq. 2.40, $Q = 1.53\,\text{MeV}$, and $\ell = 3$.

2.1.6 Spin-Orbit Interaction

So far, it has been assumed that l is a good quantum number in the nucleus. This is however not the case in general, since the orbital angular momentum $\mathbf{l}$ couples to the spin $\mathbf{s}$, which adds a spin-orbit term, V_{LS}, to the nuclear potential. Consequently, each single particle energy level splits in two, depending on the projection of $\mathbf{s}$ (this may be either $+1/2$ or $-1/2$ for a fermion).

In a spherically symmetric nucleus, the spin-orbit term may be parameterised as [6, p. 59]

$$V_{LS}(r) = \lambda \frac{1}{r} \frac{\partial V_{SO}(r)}{\partial r} \mathbf{l} \cdot \mathbf{s}, \tag{2.41}$$

where λ is the coupling strength of the spin-orbit interaction,

$$\mathbf{l}\cdot\mathbf{s} = \begin{cases} \ell/2, & j = \ell + \frac{1}{2} \\ -(\ell+1)/2, & j = \ell - \frac{1}{2}, \end{cases} \tag{2.42}$$

where j is the total angular momentum, and $V_{SO}(r)$ is the central field potential of the nucleus. For a proton, $V_{SO}(r) = V_{WS}(r) + V_C(r)$, where

$$V_{WS}(r) = -\frac{V_0}{1+\exp((r-R)/a)}, \tag{2.43}$$

and $V_C(r)$ is defined by Eq. 2.7. Therefore,

$$\frac{1}{r}\frac{\partial V_{SO}(r)}{\partial r} = \frac{V_0}{ar}\frac{1}{2+\cosh((r-R)/a)} - \frac{Ze^2}{4\pi\epsilon_0}\min\left(\frac{1}{R^3}, \frac{1}{r^3}\right). \tag{2.44}$$

In the case of a modified harmonic oscillator potential, which is another model commonly used for the nuclear potential, [6, pp. 58-61]

$$\frac{1}{r}\frac{\partial V_{HO}(r)}{\partial r} = M\omega_0^2, \tag{2.45}$$

and

$$V_{LS,HO} = -2\kappa\hbar\omega_0\mathbf{l}\cdot\mathbf{s}, \tag{2.46}$$

where ω_0 is the frequency of the harmonic oscillator, and κ is a parameter for the $\mathbf{l}\cdot\mathbf{s}$ coupling strength. Assuming $V_{LS} = V_{LS,HO}$, gives the relation

$$-2\kappa\hbar\omega_0\mathbf{l}\cdot\mathbf{s} = \lambda M\omega_0^2\mathbf{l}\cdot\mathbf{s} \Leftrightarrow \lambda = -\frac{2\kappa\hbar}{M\omega_0}. \tag{2.47}$$

For protons, the oscillator energy $\hbar\omega_0$ may be estimated as [6, p. 65]

$$\hbar\omega_0 \simeq 41\cdot A^{-1/3}\left(1 - \frac{1}{3}\frac{N-Z}{A}\right) = 41\cdot A^{-1/3}\left(\frac{2}{3} + \frac{2Z}{A}\right). \tag{2.48}$$

Thus,

$$V_{LS}(r) \simeq -\frac{2\kappa\hbar^2}{M}\frac{A^{1/3}}{41\left(\frac{2}{3}+\frac{2Z}{A}\right)}\left(\frac{V_0}{ar}\frac{1}{2+\cosh((r-R)/a)} - \frac{Ze^2}{4\pi\epsilon_0}\min\left(\frac{1}{R^3}, \frac{1}{r^3}\right)\right)\mathbf{l}\cdot\mathbf{s}. \tag{2.49}$$

The proton which is emitted in ^{53}Co, is in the $1f_{7/2}$ nuclear subshell; thus, $n = 0$ and $\ell = 3$. The principal quantum number is defined as [6, p. 78]

$$N = 2n + \ell, \tag{2.50}$$

so $N = 3$ in this case. Following [6, p. 71], $\kappa = 0.090$ at this level. The resulting spin-orbit term Eq. 2.49 was thus added to the nuclear potential, and the corresponding half-life for ^{53}Co was computed using PFA.

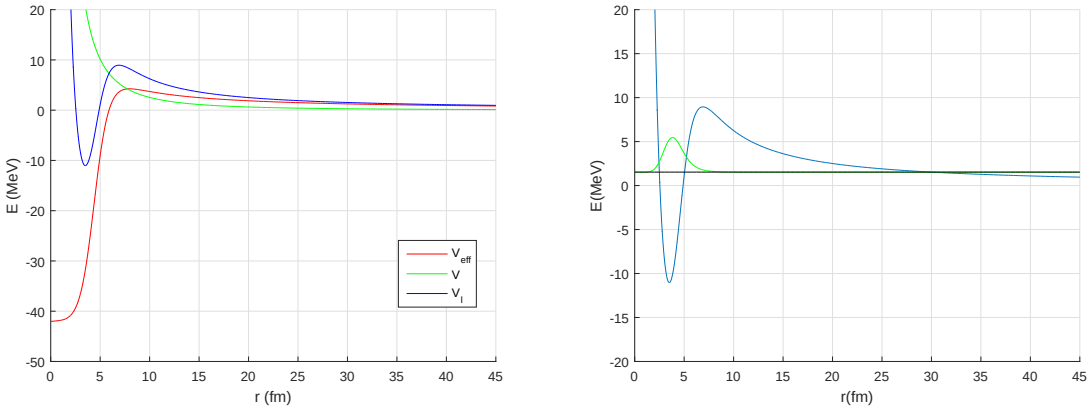

(a) **(b)**

Figure 2.1 – (a) Effective potential barrier $V_{eff}(r)$ defined by Eq. 2.6, along with the nuclear potential $V(r) = V_{WS}(r) + V_C(r)$, and the angular momentum dependent potential $V_\ell(r)$, computed for ^{53}Co using $\ell = 3$. **(b)** Effective potential barrier $V_{eff}(r)$ (blue) for ^{53}Co, along with lowest energy eigenvalue $E_1 = 1.53\,\text{MeV}$ (black), and corresponding probability density $\psi(r)^2 r^2$ plotted at E_1 (green; scaled to fit into the plot).

2.2 Results

2.2.1 Results from Different Methods

The effective potential which was used for ^{53}Co throughout Section 2.1 (except for the spin-orbit part added in Section 2.1.6), V_{eff} Eq. 2.6, divided into the individual parts $V = V_{WS} + V_C$, and the angular momentum part V_l using $l = 3$, is shown in Figure 2.1a. This potential corresponds to a potential depth $V_0 = 55.07\,\text{MeV}$. Corresponding probability density for the wave function, i.e., $\psi(r)^2 r^2$, along with proton energy E_1 and V_{eff}, are shown in Figure 2.1b. The resulting half-life in the WKB approximation was $t_{1/2} \approx 1.8 \cdot 10^{-16}\,\text{s}$, i.e., a factor of about 10^{17} from the experimental estimate of $\sim 10\,\text{s}$.

The WKB results for the isotopes ^{105}Sb, ^{113}Cs, ^{147}Tm, ^{157}Ta and ^{165}Ir are given in Table 2.1, first two columns. These agree very well with the results given in [1].

In TPA, the computed half-life for ^{53}Co was $2.0 \cdot 10^{-16}\,\text{s}$, which is similar to the value obtained for WKB. Analogous computed half-lives for ^{105}Sb, ^{113}Cs, ^{147}Tm, ^{157}Ta and ^{165}Ir are presented in Table 2.1 and compared with the results in [1]. The results all agree well with previous calculations.

Regarding PFA, comparisons of different values of $t_{1/2}$ computed both for ^{53}Co and for the reference isotopes at different grid points are given in Figure 2.2. As seen, they are all more or less constant throughout the interval. The values of $\overline{t_{1/2}}$, defined in Eq. 2.31, for ^{105}Sb, ^{113}Cs, ^{147}Tm, ^{157}Ta and ^{165}Ir are given in Table 2.1, where they are compared with the results from the WKB and the TPA methods. All calculations agree well between the different methods. For ^{53}Co, the value obtained from PFA is $1.8 \cdot 10^{-16}\,\text{s}$, which is also in good agreement with the other methods.

The computed half-life for ^{53}Co using GAMOW and the same parameters as for the other methods, was $t_{1/2} = 1.8 \cdot 10^{-16}\,\text{s}$, which is in perfect agreement with WKB and PFA, although slightly lower than the result from TPA. A summary of the values of $t_{1/2}$ for ^{53}Co obtained from different methods is given in Table 2.2.

For the iterative improvement of PFA, it turned out that the change in results for ^{53}Co was marginal.

Table 2.1 – Calculated half-lives for proton emission for some nuclei, using the WKB, TPA and PFA methods described in Sections 2.1.1, 2.1.2 and 2.1.3, respectively. These results are compared with results given in Table II in [1], when applicable, obtained by using the same methods. Note that the PFA method was not used in [1].

Nucleus	WKB		TPA		PFA
	This thesis	Ref. [1]	This thesis	Ref. [1]	
^{105}Sb	18 s	19 s	21 s	21 s	20 s
^{113}Cs	490 ns	510 ns	570 ns	570 ns	540 ns
^{147}Tm	380 ms	370 ms	400 ms	380 ms	360 ms
^{157}Ta	210 ms	210 ms	230 ms	230 ms	220 ms
^{165}Ir	120 μs	110 μs	120 μs	110 μs	100 μs

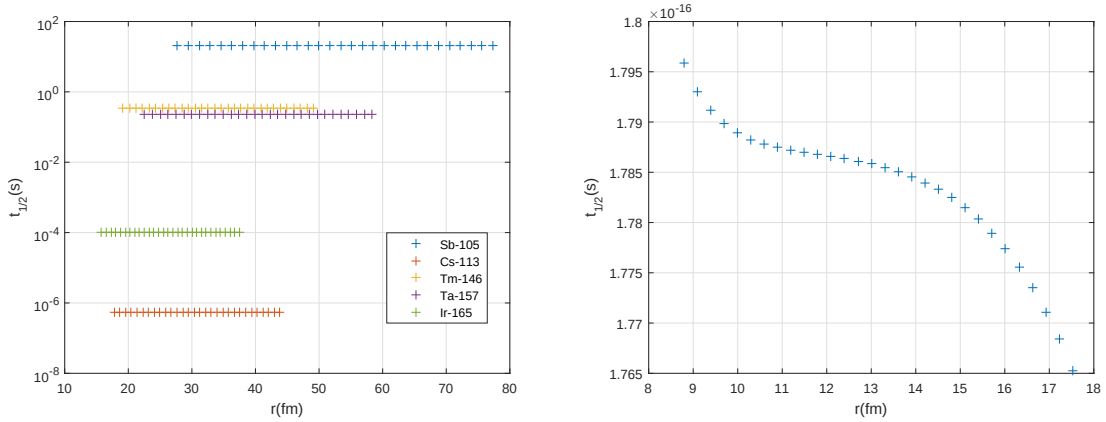

(a) **(b)**

Figure 2.2 – Evaluations of $t_{1/2}$ for different grid points on the intervals $r \in [r_1 + 0.15(r_2 - r_1), r_1 + 0.50(r_2 - r_1)]$ (different for different nuclei) using the PFA method. **(a)** Comparison between computed half-lives for ^{105}Sb, ^{113}Cs, ^{147}Tm, ^{157}Ta and ^{165}Ir. Note the logarithmic scale. **(b)** Analogous for ^{53}Co. Note: linear scale.

Table 2.2 – Half-lives for ^{53}Co obtained by each of the methods WKB, TPA, PFA and GAMOW.

Method	$t_{1/2}$ (s)
WKB	$1.80 \cdot 10^{-16}$
TPA	$2.00 \cdot 10^{-16}$
PFA	$1.79 \cdot 10^{-16}$
GAMOW	$1.78 \cdot 10^{-16}$

2.2.2 Test of Energy Window

Obtained values of $t_{1/2}$ for $Q = 1, 2, 3, 4, 5, 6, 7, 8, 9$, and 9.8 MeV for each of the methods described in Section 2.1 are plotted in Figure 2.3, along with values normalised to the ones obtained by GAMOW. As seen, the results obtained by WKB all agree very well with GAMOW, except for $Q = 9.8$ MeV. The values obtained by TPA are consistently too high. PFA typically falls in between the results from GAMOW and TPA. The original version agrees well with GAMOW at low energies, $Q \lesssim 4$ MeV. The improved version described in Section 2.1.3 is generally more accurate than the original PFA, but the values are lower than the WKB results for $Q \gtrsim 7$ MeV, and the agreement with GAMOW is poor for $Q \gtrsim 8$ MeV.

The change in energy obtained by using fixed potentials in GAMOW, as compared to the

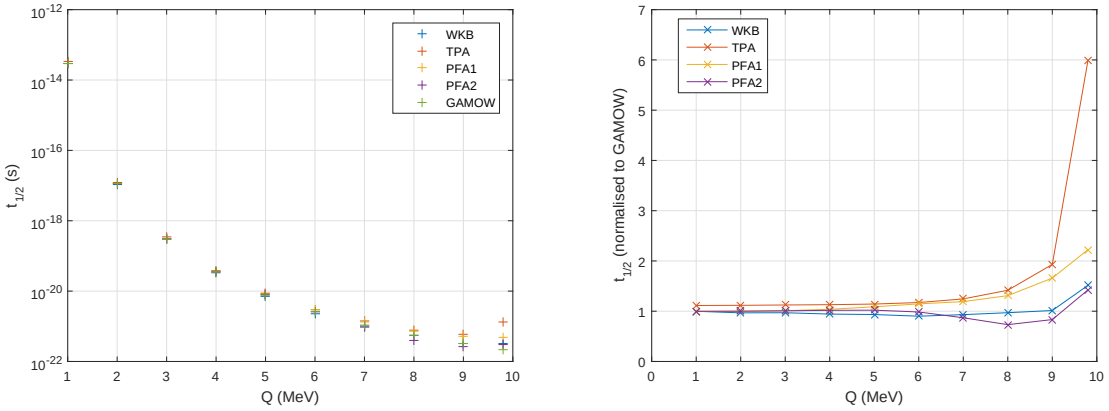

(a) **(b)**

Figure 2.3 – **(a)** Half-lives obtained from the methods WKB, TPA and PFA, as well as the code GAMOW [2] are plotted for ^{53}Co at various energy levels (computed as if there would be a resonant state with $\ell = 3$ at these levels). Here, PFA1 denotes the original version of PFA, whereas PFA2 denotes the improved version described in the end of Section 2.1.3. **(b)** Values from WKB, TPA and PFA normalised to the results obtained by GAMOW.

original results, are given in Table 2.3. As seen, there are only small changes in decay energy for $Q \lesssim 7\,\text{MeV}$, which is consistent with the high accuracy in decay time obtained by PFA for these energies. At higher energies, the energies obtained by GAMOW start to deviate significantly from my results. For the potential obtained by my programme for $Q = 9.8\,\text{MeV}$ (which is very close to the top of the barrier), GAMOW was not able to find any bound state at all.

Table 2.3 – Change in energy (ΔE) when using GAMOW for fixed potentials, obtained from Golden Section search as described in Section 2.1.3, for Q-values given in the left column. Corresponding potential depths are given in the central column. A positive sign for ΔE corresponds to an increase in energy obtained by GAMOW.

Q (MeV)	V_0 (MeV)	ΔE (keV)
1.0	55.9738	+3.4
1.53	55.0418	+3.4
2.0	54.2027	+3.3
3.0	52.3688	+3.2
4.0	50.4514	+2.0
5.0	48.4367	-7.0
6.0	46.3068	-29.5
7.0	43.8834	+15.5
8.0	40.9409	+186
9.0	36.6824	+729
9.8	31.1966	no bound state found

2.2.3 Dependence on ℓ and Z

Computed half-lives for different values of ℓ for ^{53}Co are given in Table 2.4. These indicate that an increase in ℓ by one unit increases the half-life by roughly a factor of 12. Extrapolating this to the observed angular momentum $\ell = 9$, therefore gives in increase in half-life by a factor

of $3 \cdot 10^6$, i.e., to $t_{1/2} \sim 5 \cdot 10^{-10}\,\mathrm{s}$.

Table 2.4 – Proton emission half-lives for nuclei with $Z = 27$, $A = 53$, and $Q = 1.53\,\mathrm{MeV}$, computed for different values of ℓ by using PFA.

ℓ	$t_{1/2}\,(\mathrm{s})$
1	$1.2 \cdot 10^{-18}$
2	$1.5 \cdot 10^{-17}$
3	$1.8 \cdot 10^{-16}$

Results for the dependence on A for different isotopes of cobalt are given in Figure 2.4a. These indicate quite a weak dependence on A, with a relative difference in half-life between two nuclei on the interval of $\lesssim 40\%$.

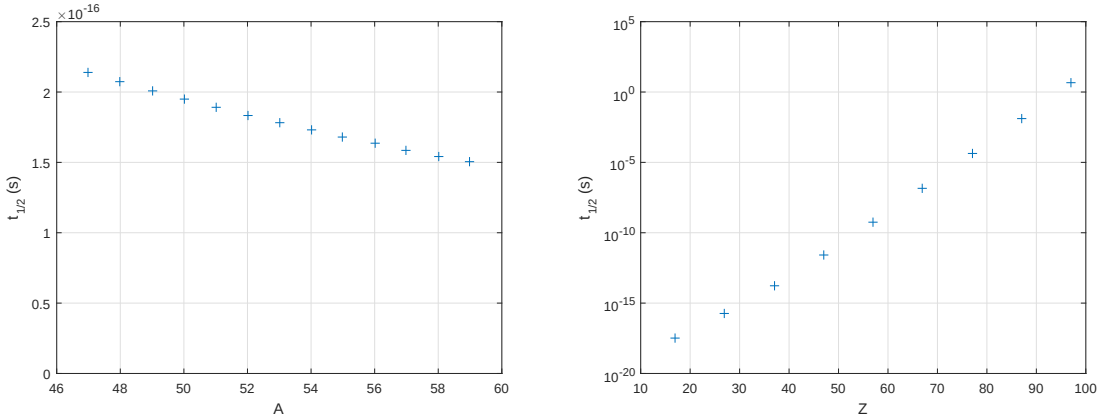

(a) **(b)**

Figure 2.4 – **(a)** Computed half-lives for cobalt ($Z = 27$) for $A \in [47, 59]$, where Q is fixed at 1.53 MeV and $\ell = 3$. **(b)** Computed half-lives for some isotopes on the interval $Z \in [17, 97]$, where A is given by Eq. 2.40, Q is fixed at 1.53 MeV, and $\ell = 3$.

The results for the Z-dependence on the half-life are given in Figure 2.4b. Due to the increase in thickness of the Coulomb barrier with increasing Z, the half-life increases by more than two orders of magnitude for each increment in Z by 10.

2.2.4 Spin-orbit Interaction

After adding the spin-orbit term defined by Eq. 2.49 to the nuclear potential, the resulting PFA half-life for ^{53}Co was $1.5 \cdot 10^{-16}\,\mathrm{s}$, i.e., a slight decrease from the result in Section 2.1.3. Moreover, the potential depth decreased to $V_0 = 49.72\,\mathrm{MeV}$.

2.3 Discussion

The half-lives calculated using each of the methods described in Section 2.1 agree very well, both for ^{53}Co and for each of the isotopes. Moreover, the results for the reference isotopes agree well with the results in [1] and the results for ^{53}Co agree well with the results obtained by GAMOW, which were computed using a different approach. Therefore, I conclude that all calculations in 2.1 are indeed correct and that the methods WKB, TPA and PFA are interchangeable for a simple, spherical symmetric model, at least for states with a Q-value

well below the height of the potential barrier. This also validates that PFA may be used to compute half-lives for proton emission, which has likely not been tested before.

The iterative approach described in Section 2.1.3 indeed gives improved results in most of the energy range. However, the underestimate in decay time close to the top of the potential barrier makes this method quite unpredictable. This is something which should be further studied, and may be connected to the problem with convergence at large Q-values if iterating Eq. 2.32 directly. The modified formula for computing the complex energy (Eq. 2.36) should also be validated further. If using a slightly smaller value of $\mathrm{Im}\, E$ (e.g. $\mathrm{Im}\, E = 0.4\hbar\lambda$), the results agreed better with WKB and GAMOW, but since the physical implication of this modification is uncertain, one should be careful with drawing any conclusions from it. Since the iterative approach was both time consuming and had a very small effect on the computed half life of ^{53}Co, this method and its shortcomings of were not investigated further.

Although the methods studied in this part all work well in a spherical model, where structural changes are not considered, at least WKB has major drawbacks. When studying deformed nuclei, the barrier thickness would be different in different directions, which would make it difficult to derive a useful equation for the barrier penetrability. Moreover, when including structural changes, the properties of the potential barrier (such as deformation) would change during decay, making this approach invalid.

When using TPA, again the solution is built on properties of the nuclear potential, which would cause similar problems as when using WKB. In particular, one needs to evaluate the wave functions at the top of the barrier of a spherically symmetric potential (cf. Eq. 2.14). Moreover, the half-lives obtained using TPA are consistently too high (cf. Table 2.1 and Figure 2.3).

On the other hand, PFA has none of the drawbacks present for WKB and TPA. Therefore, this method will be used further on in this thesis, whereas WKB and TPA are rejected.

The half-life obtained for ^{53}Co using a state with $\ell = 3$ and $Q = 1.53\,\mathrm{MeV}$ was in this part about $1.5 \cdot 10^{-16}\,\mathrm{s}$ when including the spin-orbit term (cf. Section 2.2.4). This is ~ 17 orders of magnitude lower than the experimental estimate. Here, several simplifications have been made. In particular, in order to get the observed Q-value, it is required that $\ell = 9$, and that there are large structural changes in the nucleus. Both of these requirements have here been lifted, in order to create a state which fits into this model. With $\ell = 9$, it was not possible to form a bound state in the spherical model, and structural changes have been left until later. If having a state where the change in angular momentum $\Delta\ell = 3$ between the mother and daughter nuclei, the Q-value would be negative, which can be easily seen if studying level schemes of ^{53}Co and ^{52}Fe [3]. Therefore, the situation studied in this section does not correspond to a physical situation, and a refined model is required.

To get a measure of how much an increase in angular momentum to $\ell = 9$ would affect the results, one may study Table 2.4. This indicates that – mostly due to the increased thickness of V_{eff} – the half-life increases by a factor of ~ 12 for each increment in ℓ. Extrapolating this to $\ell = 9$, thus gives an increase in half-life to $\sim 4.5 \cdot 10^{-10}\,\mathrm{s}$.

The number of protons in the nucleus is a much more significant factor for the decay time of proton emission, than the number of neutrons. The reason for this is that the thickness of the Coulomb barrier increases with increased nuclear charge. Therefore, lighter nuclei, such as ^{53}Co, are expected to decay much faster in the proton branch than heavier nuclei, if excluding effects from structural changes.

Chapter 3

Inclusion of Structural Changes: the Nuclear Pairing Interaction

In order to take into account changes in nuclear structure, a treatment of the nuclear pairing interaction is included in this part. This is an interaction which favours pairs of protons and neutrons, and as a consequence, nuclear states are not pure single particle states at a certain energy, but are rather superpositions of single particle states with different energies. Such a superposition is called a quasiparticle. In this description, the mother nucleus being subject to proton emission may be described as a quasiparticle excitation of the daughter nucleus, and excited states may be formed by adding additional quasiparticles. By using this treatment, the overlap between the mother and the daughter nucleus may be calculated, which adds additional factors to the PFA method described in Section 2.1.3.

3.1 Methods

3.1.1 Basic Theory

Due to the pairing interaction, which is described in detail in [6, pp. 290-321], the distribution of nucleons in a nucleus follow a Fermi distribution. This means that the unpaired energy states for a given type of particles (i.e., protons or neutrons) mix. Consequently, each state in a nucleus with n energy levels is a superposition of up to n unpaired eigenstates. These eigenstates are called particle states. Moreover, since the number of nucleons is smaller than the number of energy levels, one may also define hole states, which are complementary to the particle states. A superposed state of n particle states and n hole states, is called a *quasiparticle* state.

Now denote the probability amplitude for a particle at energy level i to be in the energy eigenstate j by V_{ij} and the corresponding hole amplitude by U_{ij}. By extending these amplitudes to all indices i and j, one may construct the matrices

$$U = (U_{ij}), \qquad V = (V_{ij}). \tag{3.1}$$

The particle and hole probabilities for each quasiparticle are then given by the diagonal values of $V^H V$ and $U^H U$, respectively. Since the total probability must be equal to one, it is required that [9, p. 246]

$$U^H U + V^H V = \mathbf{1}. \tag{3.2}$$

In practice, the pairing interaction arises by adding an interaction term Δ, which mixes particle and hole states, to the Hamilton operator. By adding this interaction, it is however

no longer guaranteed that the particle number is conserved. This is resolved by adding a Lagrange multiplier, λ, to the Hamiltonian. Physically, λ defines the Fermi level of the nucleus [6, p. 304]. Since both particle and hole states need to be included in the full Hamiltonian, this consists of $2n$ states. The resulting eigenvalue problem may be written as [9, p. 254]

$$\begin{pmatrix} \mathbf{h} & \mathbf{\Delta} \\ \mathbf{\Delta}^H & -\mathbf{h} \end{pmatrix} \begin{pmatrix} U_i \\ V_i \end{pmatrix} = E_i \begin{pmatrix} U_i \\ V_i \end{pmatrix}, \tag{3.3}$$

where

$$U_i = \begin{pmatrix} U_{1i} \\ \vdots \\ U_{ji} \\ \vdots \\ U_{ni} \end{pmatrix}, \qquad V_i = \begin{pmatrix} V_{1i} \\ \vdots \\ V_{ji} \\ \vdots \\ V_{ni} \end{pmatrix}, \tag{3.4}$$

and only positive (or negative) eigenvalues E_i are taken into account. These equations Eq. 3.3 are called the Hartree-Fock-Bogoliubov (HFB) equations. By solving these, the matrices U and V are constructed. Following the convention of [10, pp. 223-225],

$$\mathbf{h}_{ij} = (E_i^0 - \lambda)\delta_{ij}, \tag{3.5}$$

where δ is a Kronecker delta, and E_i^0 are energy eigenvalues of the original Hamiltonian. Similarly [10, p. 237],

$$\mathbf{\Delta}_{ij} = \Delta \cdot (-1)^{\alpha+\Omega}\delta_{i\bar{j}}, \tag{3.6}$$

where α is either $\frac{1}{2}$ or $-\frac{1}{2}$ (in the end, it turns out that the choice of sign does not matter), Ω is the projection of the angular momentum vector $\mathbf{j}$ along the z axis, and Δ is a constant. Moreover, $\bar{j}$ is the index of the state conjugate to state j. In order to satisfy the unitarity requirements [9, p. 246]

$$\begin{aligned} U^H U + V^H V &= \mathbf{1}, \\ U^T V + V^T U &= \mathbf{0}, \end{aligned} \tag{3.7}$$

$\mathbf{\Delta}$ must be skew-symmetric. This may be resolved by letting $\bar{j}$ states have opposite spin projections to states j.

The pairing gap Δ may e.g. be obtained by solving the gap equation described in [6, p. 305], when applicable. For many nuclei, one may make the approximation (in particular for nuclei with even Z)

$$\Delta = \frac{12}{\sqrt{A}}. \tag{3.8}$$

For spherically symmetric nuclei, $\Omega = m$, where m is the angular momentum projection. Since m has integer spacing, the phase can be chosen such that $\mathbf{\Delta}_{i\bar{j}}$ is real with alternating sign.

The particle number is given by (Eq. (6.53) in [9, p. 231] applied to Eq. (7.7-7.9) in [9, pp. 246-247])

$$\langle \mathcal{N} \rangle = \mathrm{tr}(V^H V). \tag{3.9}$$

This needs to be kept at the correct number of particles, i.e., $\langle \mathcal{N} \rangle = Z$ (number of protons in the daughter nucleus), which is done by solving Eq. 3.3 iteratively, and minimising the corresponding value of $|\langle \mathcal{N} \rangle - Z|$ with respect to λ.

3.1.2 Practical Computations

In order to solve the HFB equations, one needs to find all energy levels of the desired nucleus, along with their degeneracy, which is

$$g = 2j + 1. \tag{3.10}$$

The energy levels were found by starting from the potential V_{eff} given by Eq. 2.6 using the value of V_0 obtained in Section 2.1.6, and adding a spin-orbit term defined by Eq. 2.49. This was repeated – using the same value of V_0 – for $j = \ell \pm 1/2$, for all $\ell \in \mathbb{Z}$ for which a potential barrier appears. This was done to include all bound states in the HFB Hamiltonian. The Schrödinger equation was then solved for the modified potential $\bar{V} = V_{eff}(\ell, j) - V_{min}(\ell, j)$, where the function over ℓ and j denotes that Eq. 2.6 and Eq. 2.49 are computed for different (ℓ, j). Moreover

$$V_{min}(\ell, j) \equiv \min\left\{V_{eff}(\ell, j); r < r_{max}\right\}, \tag{3.11}$$

where r_{max} is defined in Section 2.1.1. This subtraction was done to put the potential minimum at $E = 0$, which was necessary to find bound states with negative energy in the nuclear potential. Otherwise the MATLAB routine used for solving the Schrödinger equation only finds states with $E > 0$.

When solving the Schrödinger equation, the approach used in Section 2.1.3 was used, and only wave functions with maxima within the barrier were accepted. In order to obtain the correct energy levels, $V_{min}(\ell, j)$ was added to each of the resulting energy eigenvalues. Moreover, κ was adjusted to match the current energy level, following Table 6.2 in [6, p. 71], and using Eq. 2.50. The quantum number n was found by counting bound states of the same ℓ and j. Then, the state with m:th lowest energy (starting at $m = 0$) has quantum number $n = m$. Resulting energies, along with their degeneracies, were compared with states from an estiblished nuclear model, the modified harmonic oscillator model [6, pp. 59-61].

To construct the HFB Hamiltonian, the energy levels E_i were duplicated with the corresponding degeneracy, and sorted. In this way, an initial guess for λ was obtained as $\lambda \in (E_Z + E_{Z+1})/2 \pm 2\,\mathrm{MeV}$, which was refined by minimising $|\langle \mathcal{N} \rangle - Z|$ using 19 iterations of Golden Section search by solving Eq. 3.3 repeatedly. Only positive eigenvalues were used to construct U and V. The final values of U and V were used to evaluate the significance of pairing to the decay time.

3.1.3 Effect on Half-Life Due to Pairing

Theory

To determine how the pairing interaction affects the decay time for a nucleus undergoing proton emission, one may derive an expression for the probability flow when pairing is included, and use this to calculate the half-life (cf. Section 2.1.3). For α decay, the probability amplitude at a distance r from the nucleus may be obtained by computing the projection between the mother nucleus, and the combined wavefunction of the daughter nucleus and the α particle, computed at distance r. For a mother nucleus with angular momentum J, a daughter nucleus with angular momentum j, and an α particle with angular momentum ℓ this projection integral may be written as [8]

$$g^J_{j\ell}(r,t) = A_\alpha \int \sum_m C^{JM}_{\ell m, j(M-m)} Y_{\ell m}(\Omega) \Psi_{j(M-m)}(\eta) \Upsilon_\alpha(\xi) \Phi^*_{JM}(\mathbf{x}_1, \ldots, \mathbf{x}_A, t) d\xi d\eta d\Omega. \tag{3.12}$$

Here,

$$A_\alpha = \left(\begin{pmatrix} Z \\ 2 \end{pmatrix} \begin{pmatrix} N \\ 2 \end{pmatrix} \right)^{1/2} \tag{3.13}$$

is a factor required to make the wave function antisymmetric, $C^{JM}_{\ell m,j(M-m)}$ are Clebsch-Gordan coefficients, $Y_{\ell m}(\Omega)$ are spherical harmonics for the α particle wave function, $\Upsilon_\alpha(\xi)$ is the intrinsic wave function of the α particle, $\Psi_{j(M-m)}(\eta)$ is the wave function of the daughter nucleus, and $\Phi_{JM}(\mathbf{x}_1,\ldots,\mathbf{x}_A,t)$ is the wave function of the mother nucleus. The coordinates $(\mathbf{x}_1,\ldots,\mathbf{x}_A)$ are functions of (r,ξ,η,Ω) and include summations of all spin components. The quantum number M is chosen such that $C^{JM}_{\ell m,j(M-m)}$ is non-zero for some values of m. For a resonant state, as is the case here,

$$\Phi_{JM}(\mathbf{x}_1,\ldots,\mathbf{x}_A,t) = \Phi_{JM}(\mathbf{x}_1,\ldots,\mathbf{x}_A)\exp\left(-\frac{i}{\hbar}(E-i2\Gamma)t\right), \tag{3.14}$$

so $g^J_{j\ell}(r,t)$ may be separated into

$$g^J_{j\ell}(r,t) = g^J_{j\ell}(r)\exp\left(-\frac{i}{\hbar}(E-i2\Gamma)t\right). \tag{3.15}$$

Since proton emission is very similar to α decay, the same method may be applied here. In this case, the situation is even somewhat simpler. In particular, the proton may be regarded as a point particle with spin $s = 1/2$. However, since the proton spin is non-zero, this couples to the orbital angular momentum, giving a total angular momentum of $j' = \ell \pm 1/2$. This also has consequences for the wave function, since the spin function couples to the spherical harmonics. Therefore, the intrinsic proton wave function (for a given m-state) may be written as

$$\Upsilon_p(\xi,\Omega) = \delta(\xi)[Y_\ell(\Omega),\chi]_{j'm}, \tag{3.16}$$

where the subscript p is used to emphasise that this is a proton wave function, χ_{m_s} is the spin wave function of the proton ($m_s = \pm 1/2$), and

$$[Y_\ell(\Omega),\chi]_{j'm} \equiv \sum_{m_\ell,m_s} C^{j'm}_{\ell m_\ell,\frac{1}{2}m_s} Y_{\ell m_\ell}(\Omega)\chi_{m_s}. \tag{3.17}$$

Moreover, the resulting wave function is already antisymmetric; thus $A_p = 1$. By evaluating the projection integral Eq. 3.12 over the same set of coordinates for all particles, the probability amplitude for the proton turns into

$$\begin{aligned} g^J_{jj'\ell}(r) = \int \sum_m C^{JM}_{j'm,j(M-m)}[Y_\ell(\Omega_A),\chi]_{j'm}\frac{\delta(r_A-r)}{r_A^2}\Psi_{j(M-m)}(\mathbf{x}_1,\ldots,\mathbf{x}_{A-1}) \\ \Phi^*_{JM}(\mathbf{x}_1,\ldots,\mathbf{x}_A)d\mathbf{x}_1\ldots d\mathbf{x}_A. \end{aligned} \tag{3.18}$$

Here, r_A is the radial coordinate of $\mathbf{x}_A$, Ω_A is the angular coordinate of $\mathbf{x}_A$, and the division by r_A^2 is required since the probability density decreases by r^2 in spherical coordinates. This is compensated for by the Jacobian.

Expanding Υ_p in basis functions $R_{N\ell}(r_A)[Y_\ell(\Omega),\chi]_{jm}$, where the radial part is obtained by solving the radial Schrödinger equation for different ℓ, yields

$$\Upsilon_p(r,r_A,\Omega_A) = \sum_{N\ell jm} R_{N\ell}(r_A)[Y_\ell(\Omega_A),\chi]_{jm}\left\langle R_{N\ell}(r_A)[Y_\ell(\Omega_A),\chi]_{jm}|\Upsilon_p(r,r_A,\Omega_A)\right\rangle, \tag{3.19}$$

where

$$\begin{aligned} \langle R_{N\ell}(r)[Y_\ell(\Omega),\chi]_{jm}|\Upsilon_p(r',r,\Omega)\rangle &= \int_{\mathbb{R}^3} R^*_{N\ell}(r)[Y_\ell(\Omega),\chi]^*_{jm}\frac{\delta(r-r')}{r^2}[Y_{\ell'}(\Omega),\chi]_{j'm'}r^2 dr d\Omega \\ &= R^*_{N\ell}(r')\delta_{jj'}\delta_{mm'}\delta_{\ell\ell'}. \end{aligned} \tag{3.20}$$

Here, different N correspond to eigenstates of different energy; if using a harmonic oscillator basis, N is the principal quantum number. Moreover, δ denotes a Kronecker delta, and a different convention for the quantum numbers has been used than above. Furthermore, it has been used that $[Y_\ell(\Omega), \chi]_{jm}$ form an orthonormal basis. Thus,

$$\Upsilon_p(r, r_A, \Omega_A) = \sum_N R^*_{N\ell}(r) R_{N\ell}(r_A)[Y_\ell(\Omega_A), \chi]_{j'm}, \tag{3.21}$$

where again the same convention as in Eq. 3.18 has been used.

Inserting Eq. 3.21 into Eq. 3.18, then yields

$$g^J_{jj'\ell}(r) = \sum_{m,N} C^{JM}_{j'm,j(M-m)} R^*_{N\ell}(r) \int \Phi^*_{JM}(\mathbf{x}_1, \ldots, \mathbf{x}_A) \\ \Psi_{j(M-m)}(\mathbf{x}_1, \ldots, \mathbf{x}_{A-1}) R_{N\ell}(r_A)[Y_\ell(\Omega_A), \chi]_{j'm} d\mathbf{x}_1 \ldots d\mathbf{x}_A. \tag{3.22}$$

Here, the wave function $R_{N\ell}(r_A)[Y_\ell(\Omega_A), \chi]_{jm}$ is identified as the wave function of the emitted proton, with respect to the nucleus. Using the short hand notations $|M_{JM}\rangle$ for the wave function of the mother nucleus, $|D_{j(M-m)}\rangle$ for the wave function of the daughter nucleus, and $|p_{Nj'\ell m}\rangle$ for the proton wave function, Eq. 3.22 simplifies into

$$g^J_{jj'\ell}(r) = \sum_{m,N} C^{JM}_{j'm,j(M-m)} R^*_{N\ell}(r) \langle M_{JM} | D_{j(M-m)} \otimes p_{Nj'\ell m} \rangle . \tag{3.23}$$

The emitted proton can be regarded as a particle created in the $|N\ell j'm\rangle$ subshell of the daughter nucleus. Thus,

$$|D_{j(M-m)} \otimes p_{Nj'\ell m}\rangle = a^\dagger_{N\ell j'm} |D_{j(M-m)}\rangle , \tag{3.24}$$

where $a^\dagger$ is a particle creation operator. This gives the general result

$$g^J_{jj'\ell}(r) = \sum_{m,N} C^{JM}_{j'm,j(M-m)} R^*_{N\ell}(r) \langle M_{JM} | a^\dagger_{N\ell j'm} | D_{j(M-m)} \rangle . \tag{3.25}$$

To compute the overlap integral, one may make a few different approximations. By assuming spherical symmetry in both mother and daughter nuclei (I will later leave this assumption), that the pairing interaction strength $\Delta_{mother} = \Delta_{daughter}$, and that $j = 0$ for the daughter nucleus, which is the case for ^{52}Fe, the mother nucleus may be regarded as a quasiparticle excitation of the daughter nucleus. Then

$$|M_{JM}\rangle = \beta^\dagger_k |D_{00}\rangle , \tag{3.26}$$

with the quasiparticle creation operator $\beta^\dagger_k$ defined as [9, p. 246]

$$\beta_k = \sum_l U^*_{lk} a_l + V^*_{lk} a^\dagger_l, \tag{3.27}$$

where U and V are defined in Eq. 3.4. This creates a quasiparticle at a desired orbital k in the nucleus, i.e., at correct energy and angular momentum. In this case,

$$C^{JM}_{j'm,0(M-m)} = \delta_{Mm}\delta_{Jj'},$$

where δ denotes a Kronecker delta, so

$$|g^J_{0j'\ell}(r)|^2 = \left| \sum_N R^*_{N\ell}(r) \langle D_{00} | \beta_k a^\dagger_{N\ell j'm} | D_{00} \rangle \right|^2 \delta_{Mm}\delta_{Jj'} \tag{3.28}$$

for a given orbital k. Moreover, there is an inverse relation to 3.27, which reads as [9, p. 246]

$$a_l^\dagger = \sum_k U_{lk}^* \beta_k^\dagger + V_{lk} \beta_k. \tag{3.29}$$

Since the daughter nucleus is a BCS (Bardeen-Cooper-Schrieffer) vacuum state, i.e, a quasiparticle vacuum state, the following relations hold [6, pp. 294 & 320]:

$$\langle D_{00} | \beta_\mu \beta_\nu^\dagger | D_{00} \rangle = \delta_{\mu\nu}, \tag{3.30}$$

and

$$\beta_\nu \left| D_{00} \right\rangle = \left| null \right\rangle. \tag{3.31}$$

Using these relations and Eq. 3.29, one obtains

$$\langle D_{00} | \beta_k a_{N\ell j' m}^\dagger | D_{00} \rangle = U_{N\ell j' m,k}^*, \tag{3.32}$$

which is known as the *spectroscopic factor*, and Eq. 3.28 reduces to

$$|g_{0j'\ell}^J(r)|^2 = \left| \sum_N R_{N\ell}^*(r) U_{N\ell j' m,k}^* \right|^2 \delta_{Jj'}. \tag{3.33}$$

More generally, one may define a mother nucleus $|\tilde{M}_{JM}\rangle$, which is defined by basis states in the mother nucleus, and satisfies

$$\left| \tilde{M}_{JM} \right\rangle = \tilde{\beta}_k^\dagger \left| \tilde{D}_{00} \right\rangle, \tag{3.34}$$

where $\tilde{\beta}_k^\dagger$ is a quasiparticle creation operator in the common basis of $|\tilde{M}_{JM}\rangle$ and $|\tilde{D}_{00}\rangle$. Then the overlap is

$$\begin{aligned} &\langle \tilde{M}_{JM} | a_{N\ell j' m}^\dagger | D_{00} \rangle = \langle \tilde{D}_{00} | \tilde{\beta}_k a_{N\ell j' m}^\dagger | D_{00} \rangle \\ &= \sum_i \langle \tilde{D}_{00} | \left(\tilde{U}_{ik}^* a_i + \tilde{V}_{ik}^* a_i^\dagger \right) a_{N\ell j' m}^\dagger | D_{00} \rangle. \end{aligned} \tag{3.35}$$

In order to compute this overlap, one may use the relations [9, p. 619]

$$\begin{aligned} \langle \tilde{D} | a_l^\dagger a_k | D \rangle &= \langle \tilde{D} | D \rangle \left(V^* \left(U^H \tilde{U} + V^H \tilde{V} \right)^{T^{-1}} \tilde{V}^T \right)_{kl}, \\ \langle \tilde{D} | a_l a_k | D \rangle &= \langle \tilde{D} | D \rangle \left(V^* \left(U^H \tilde{U} + V^H \tilde{V} \right)^{T^{-1}} \tilde{U}^T \right)_{kl}, \\ \langle \tilde{D} | a_l^\dagger a_k^\dagger | D \rangle &= - \langle \tilde{D} | D \rangle \left(U^* \left(U^H \tilde{U} + V^H \tilde{V} \right)^{T^{-1}} \tilde{V}^T \right)_{kl}, \end{aligned} \tag{3.36}$$

along with the anticommutator relation for fermions, [6, p. 294]

$$\left\{ a_\mu, a_\nu^\dagger \right\} = \delta_{\mu\nu}. \tag{3.37}$$

Applying these relations to Eq. 3.35 then yields

$$\begin{aligned} &\langle \tilde{M}_{JM} | a_{N\ell j' m}^\dagger | D_{00} \rangle \\ &= \langle \tilde{D}_{00} | D_{00} \rangle \left(\tilde{U}_{N\ell j' m,k}^* - \left(\tilde{V} \left(U^H \tilde{U} + V^H \tilde{V} \right)^{-1} \left(V^H \tilde{U}^* + U^H \tilde{V}^* \right) \right)_{N\ell j' m,k} \right) \end{aligned} \tag{3.38}$$

In this way, the overlap integral $\langle \tilde{M}_{JM} | a^\dagger_{N\ell j' m} | D_{00} \rangle$ reduces to compute the overlap between two states of equally many particles. This may be done by using the Onishi formula [9, p. 618], which in this case is formulated as

$$\langle \tilde{D}_{00} | D_{00} \rangle = \sqrt{\det(U^H \tilde{U} + V^H \tilde{V})}. \tag{3.39}$$

Therefore, a generalisation of Eq. 3.33 is

$$\begin{aligned} |g^J_{0j'\ell}(r)|^2 &= \left| \det(U^H \tilde{U} + V^H \tilde{V}) \right| \\ &\cdot \left| \sum_N R^*_{N\ell}(r) \left(\tilde{U}^*_{N\ell j' m,k} - \left(\tilde{V} \left(U^H \tilde{U} + V^H \tilde{V} \right)^{-1} \left(V^H \tilde{U}^* + U^H \tilde{V}^* \right) \right)_{N\ell j' m,k} \right) \right|^2 \delta_{Jj'}. \end{aligned} \tag{3.40}$$

The function $g^J_{jj'\ell}(r)$ is interpreted as a probability amplitude, and may therefore be used to calculate the probability flow. Therefore, $|\psi(r)|^2$ may be replaced by $|g^J_{jj'\ell}(r)|^2$ in Section 2.1.3 to compute the half-life when taking pairing into account.

In practice, each of the energy levels is degenerate due to different angular momentum projections. Therefore, it is impossible to deduce the m quantum number of the daughter nucleus, and different $\tilde{U}^*_{N\ell j' m,k}$ mix in an unpredictable way. This was resolved by slightly modifying the elements in the pairing Hamiltonian in Eq. 3.3 to

$$\mathbf{h}_{ij} = \mathbf{h}^0_{ij} + \epsilon m_i \delta_{ij}, \tag{3.41}$$

where $\mathbf{h}^0$ is the original Hamilton operator, ϵ is an infinitesimal constant, and m_i is the m quantum number corresponding to state i (degenerate states have different m). This splits states with different m, and therefore only one component in U and V, respectively, contributes to the sum in Eq. 3.40.

Applications to ^{53}Co

For ^{53}Co, the valence proton is in the $1f_{7/2}$ subshell, i.e., the proton wave function has $j = 7/2$ and $\ell = 3$. The daughter nucleus, ^{52}Fe, is on the other hand in its 0^+ ground state [3], meaning that $j = \ell = 0$ for this nucleus. So far, I have neglected the influence of neutrons, which is an over-simplification, since the neutrons have $j = 6$ in the mother nucleus, and this angular momentum is transferred to the proton during the decay process. This requires some special treatment for the neutrons, and will therefore be postponed until later. Neglecting the influence of neutrons, it is therefore assumed that the emitted proton has total angular momentum $j = 7/2$. With this assumption, Eq. 3.33 transforms into

$$\left| g^{\frac{7}{2}}_{0\frac{7}{2}3}(r) \right|^2 = \left| \sum_N \psi^*(r) U^*_{N3\frac{7}{2}M,k} \right|^2 \tag{3.42}$$

in this treatment, where k denotes a state at the 1.53 MeV level. Here, I have used that the radial wave function is simply $\psi(r)$, as defined in Section 2.1.1, for all states at $E = 1.53$ MeV. Moreover, only one value of N contributes to this level, which is a consequence of finding (within numerical precision) exact solutions to the Hamilton operator using a Woods-Saxon potential, instead of expanding the solution in some basis. In this particular case,

$$|g^J_{jj'\ell}(r)|^2 = C \cdot |\psi(r)|^2.$$

Here, $C > 0$ is the constant of proportionality, which means that the half-life increases by a factor of $1/C$ when taking pairing into account.

Three different models for pairing were tested. In the first model, the pairing interaction is neglected, i.e., $\Delta = 0$, to check that this method reproduces the results in Section 2.1.3. In the second model, $\Delta = 12/\sqrt{A}$ as motivated in Section 3.1.1. In the third one,

$$\Delta_{odd} = x \cdot \Delta_{even}, \qquad 0 \leq x \leq 1, \tag{3.43}$$

where Δ_{odd} is used for odd-even nuclei (here ^{53}Co), and Δ_{even} for even-even nuclei (here ^{52}Fe), to illustrate that the pairing interaction is weaker in odd-even nuclei than in even-even nuclei. According to Gillis Carlsson, a realistic value is $x \approx 0.8$.

In the first case, the HFB equations Eq. 3.3 are diagonal, and thus the energy eigenvalues are given by $h_{ii} = E_i^0 - \lambda$, with the basis vectors as eigenvectors. Only selecting $E_i = h_{ii} > 0$ implies that

$$U_{ij} = \begin{cases} \delta_{ij}, & E_i^0 > \lambda \\ 0, & E_i^0 < \lambda. \end{cases} \tag{3.44}$$

Here, one cannot really use the same approach as above, since the Fermi level is located at $\lambda = 1.53\,\text{MeV}$, i.e, directly at the $1f_{7/2}$ energy level. In order to conserve particle number, six states need to be occupied, and the remaining two are not. Thus, the emitted proton must be created at one of these levels, and

$$\left| g^{\frac{7}{2}}_{0\frac{7}{2}3}(r) \right|^2 = |\psi(r)|^2, \tag{3.45}$$

which is the same result as in Section 2.1.3. This validates the derivation in Section 3.1.3.

In the second case, Golden Section search was used to find a Fermi level which preserves the particle number Eq. 3.9, and then using Eq. 3.42 to compute the corresponding increase in half-life relative to the value obtained in Section 2.1.3.

In the third case, $\tilde{U}$ and $\tilde{V}$ were computed for different values of $x \in [0, 1]$, and the resulting projection integrals and corresponding increases in half-life were computed using Eq. 3.40. Due to numerical problems when setting $x = 0$, $x = 5 \cdot 10^{-4}$ was used as the lowest value. Particular attention was taken to the realistic value of $x \approx 0.8$.

3.2 Results

The energies of all bound states in ^{53}Co, which were later used for solving the HFB equations Eq. 3.3, along with their degeneracies, are given in Table 3.1. Here, two observations are made. First, if neglecting pairing, the highest filled level corresponds to the $\ell = 3$ state, where the proton subject to proton emission is supposed to be. Second, the positions of states with negative energy agree well with existing nuclear models, reproducing the magic numbers (see e.g. Figure 6.3 in [6, p. 60]). On the contrary, for positive energies, which correspond to quasi-bound states, the spectrum is more dense, and these levels do not correspond to the magic numbers.

When using the pairing gap $\Delta = 12/\sqrt{A}$ in the HFB equations 3.3, the particle number 3.9 was preserved for $\lambda = 0.71\,\text{MeV}$. Using this value of λ, the obtained probability density Eq. 3.42 is

$$\left| g^{\frac{7}{2}}_{0\frac{7}{2}3}(r) \right|^2 = 0.723 \cdot |\psi(r)|^2,$$

which gives an increase in half-life by a factor of 1.38 relative to the PFA result given in Section 2.2.4, yielding the result $t_{1/2} = 2.1 \cdot 10^{-16}\,\text{s}$.

Table 3.1 – Computed energy levels in ^{53}Co, along with corresponding angular momentum quantum numbers ℓ, j, and degeneracies.

E (MeV)	ℓ	j	Degeneracy
-25.5	0	1/2	2
-17.2	1	3/2	4
-13.7	1	1/2	2
-8.1	2	5/2	6
-4.5	0	1/2	2
-2.4	2	3/2	4
+1.5	3	7/2	8
+2.4	1	3/2	4
+2.5	3	7/2	8
+2.8	3	7/2	8
+3.3	1	3/2	4
+3.3	0	1/2	2

E (MeV)	ℓ	j	Degeneracy
+3.4	1	1/2	2
+3.7	1	3/2	4
+4.3	1	1/2	2
+4.8	1	3/2	4
+5.0	1	1/2	2
+6.3	2	5/2	6
+6.8	3	5/2	6
+7.1	3	5/2	6
+8.7	3	5/2	6
+10.8	4	9/2	10
+12.1	4	9/2	10

Resulting overlaps $\langle \tilde{D}_{00} | D_{00} \rangle$ and spectroscopic factors when using different values of Δ in the mother nucleus than in the daughter nucleus are shown in Figure 3.1. For the realistic value $\Delta_{mother} = 0.8\Delta_{daughter}$, $\langle \tilde{D}_{00} | D_{00} \rangle = 0.984$. At this level, the spectroscopic factor

$$\left| \tilde{U}^*_{N3\frac{7}{2}M,k} - \left(\tilde{V} \left(U^H \tilde{U} + V^H \tilde{V} \right)^{-1} \left(V^H \tilde{U}^* + U^H \tilde{V}^* \right) \right)_{N3\frac{7}{2}M,k} \right|^2 = 0.725, \tag{3.46}$$

i.e., almost identical to using $\Delta_{mother} = \Delta_{daughter}$, resulting in an increase in $t_{1/2}$ by a factor of 1.42 from the original value, again resulting in $t_{1/2} = 2.1 \cdot 10^{-16}$ s. This results in a negligible difference from using the same pairing gap.

In the extreme case $x = 5 \cdot 10^{-4}$, i.e., essentially no pairing gap in the mother nucleus, $\langle \tilde{D}_{00} | D_{00} \rangle = 0.17$ and the spectroscopic factor 0.97, resulting in an increase in half-life by a factor of ~ 35, to $t_{1/2} = 5.4 \cdot 10^{-15}$ s. In this case, pairing would have quite a significant effect on the half-life.

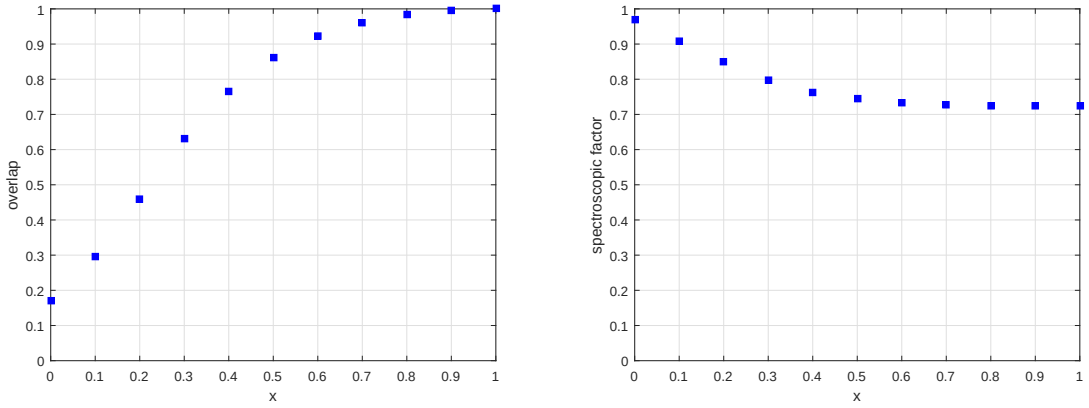

(a) **(b)**

Figure 3.1 – **(a)** Overlap $\langle \tilde{D}_{00} | D_{00} \rangle$ between the daughter nucleus ^{52}Fe, denoted by $|D_{00}\rangle$, with $\Delta = 12/\sqrt{A}$, and the mother nucleus ^{53}Co with one quasiparticle removed, denoted by $|\tilde{D}_{00}\rangle$, with $\Delta = x \cdot 12/\sqrt{A}$, as a function of x. **(b)** Spectroscopic factors defined analogously as in Eq. 3.46 for the 27th proton state in the mother nucleus, for the same situation as in **(a)**.

3.3 Discussion

When looking at the energy spectrum used for calculating the pairing overlap (Table 3.1), the magical numbers are preserved for bound states, but not for quasibound states. The reason for the latter is that unbound states form a continuous spectrum, whereas bound states appear at discrete levels. Therefore, quasibound states appear somewhere in between, with a much denser spectrum than for bound states, which is exactly what is observed.

In this part, the computed half-life did not change much from the original estimate in part 2. Nevertheless, this is an important step for taking into account structural changes in deformed nuclei, as will be seen in Section 4.1.

Using different pairing gaps in the mother and daughter nuclei, appeared for realistic differences to only have a marginal effect on the results, and it was therefore decided to neglect this effect further on. On the other hand, if there is a large difference in pairing gap between the mother and daughter nuclei, as indicated by some theoretical models (according to Gillis Carlsson), this would be a significant hindrance factor for the decay. Therefore, if doing more refined calculations, this is an effect which should be considered. Another improvement would be to compute the pairing gap using a more advanced model, such as in [9, p. 254]. For the purpose of this thesis, however, this was concluded not to be worth the effort.

Here, I should also mention the increase in spectroscopic factor observed when using a smaller pairing gap. This is most likely a consequence of the Fermi function being less smooth when decreasing the pairing gap, resulting in more well-defined particle and hole states.

Chapter 4

Deformation

So far, it has been assumed in all computations that both the mother and the daughter nucleus are spherically symmetric. This is, however, not true for nuclei which do not have closed shells. Therefore, neither ^{53}Co, nor the daughter nucleus, ^{52}Fe, are spherically symmetric. Therefore, in order to get a more accurate picture, the overlaps are in this part computed in a deformed potential. In particular, it is required to compare overlaps between nuclei for a large range of deformations, which is important since the deformation of the $I^\pi = 19/2^-$ state of ^{53}Co is unknown. With these improvements, a similar treatment as was used in Section 3.1.3, along with PFA are tested here to get an estimate for how much different effects affect the half-life of ^{53}Co.

4.1 Methods

4.1.1 Deformed Potential

Although not being spherically symmetric, the nuclei ^{53}Co and ^{53}Fe are expected to be axially symmetric. To describe axially symmetric deformed nuclei, one may use the parametrisation [11, p. 56]

$$R = R(\theta) = R_0 \left(1 + \sum_{l=2}^{\infty} \left(\beta_l Y_{l0}(\theta) - \frac{\beta_l^2}{4\pi} \right) \right), \tag{4.1}$$

for the liquid drop radius R, where $Y_{\ell m}$ are spherical harmonics. The quadratic term is introduced to take into account volume conservation. For many nuclei, the β_2 component is strongly dominant, and therefore this is the only one considered here. According to [12], $\beta_2 \approx 0.25$ for ^{52}Fe. The mother nucleus, on the other hand, is in an excited state, and therefore the deformation has not been calculated for this one. According to [13], $\beta_2 \sim 0.10 - 0.15$ for the desired excited state of ^{53}Co. As a first approach, however, β_2 was used as a free parameter, and the methods were tested for several values of $\beta_2 \in [-0.5, 0.5]$.

In the axially symmetric case, the Schrödinger equation may be written as

$$\left(-\frac{\hbar^2}{2M} \nabla^2 + V(\mathbf{r}) \right) \psi(\mathbf{r}) = E\psi((r)), \tag{4.2}$$

where $\mathbf{r} = \mathbf{r}(r, \theta)$ in spherical coordinates is the coordinate vector (there is no ϕ dependence in the axially symmetric case), and M is the nucleon mass. For simplicity, an estimate of the average nucleon mass was used in this section, $M = 938.9072\,\text{MeV}$. Compared to the reduced mass, which was used in Section 2.1, this gives a difference in energy of $\sim 0.5\,\text{MeV}$, which was expected not to have a major impact on the result, since this is a small value compared

to the nuclear potential depth. The nuclear potential V is the same as in Eq. 2.6 without the angular momentum part V_l (this term arises from the angular part of the wave function when working in spherical symmetry, cf. e.g. [6, p. 54]), except that the nuclear radius R is now a function of θ, and is defined by Eq. 4.1. If only including the β_2 term,

$$R(\theta) = R_0\left(1 + \beta_2 Y_{20}(\theta) - \frac{\beta_2^2}{4\pi}\right) = R_0\left(1 + \beta_2\sqrt{\frac{5}{16\pi}}\left(3\cos^2\theta - 1\right) - \frac{\beta_2^2}{4\pi}\right). \tag{4.3}$$

Moreover, a spin-orbit coupling term was included. In the deformed case, however, there does not exist such a simple expression for the spin-orbit coupling as the one given by Eq. 2.41. Instead, a simpler model was considered. If using a modified harmonic potential, V_{LS} is simply a constant splitting, given by Eq. 2.46. Therefore, Eq. 2.49 was replaced by this expression when working with deformed nuclei. Moreover, the same coupling constant κ was used for all levels. To summarise, the following nuclear potential was used in the deformed case:

$$V(\mathbf{r}) = -\frac{V_0}{1 + \exp((r - R(\theta))/a)} + V_C(\mathbf{r}) - 2\kappa\hbar\omega_0\mathbf{l}\cdot\mathbf{s}, \tag{4.4}$$

where V_C is given by Eq. 2.7 (except that $R = R(\theta)$) and $\mathbf{l}\cdot\mathbf{s}$ is given by Eq. 2.42.

In the axially symmetric case, it is quite difficult to use the same approach for solving the Schrödinger equation as was used in Section 2.1.1, since this is built upon radial symmetry. Instead, the Hamilton operator (for the daughter nucleus) was expanded in a spherical harmonic oscillator basis. To split energy levels of different angular momentum projection Ω, which was required to avoid problems with degenerate levels, an infinitesimal term $\epsilon\Omega\delta_{jj'}\delta_{\Omega\Omega'}$, where δ denotes a Kronecker delta, was added to the Hamiltonian, as done in Eq. 3.41.

With this modification, the resulting matrix was diagonalised to obtain the eigenstates and energy eigenvalues. The code for computing this was written by Gillis Carlsson. The number of oscillator shells used was a parameter for the code. Here, one needs to make a trade-off. Using more shells improves accuracy on the cost of speed.

4.1.2 Calculation of Half-Life in the Deformed Case

In order to compute the half-life in the deformed case, one may use the same overlap integral as in the spherical case Eq. 3.18, with the differences that the angular momenta of the mother and the daughter nuclei J and j, respectively, are no longer good quantum numbers, and that the angular momentum projection m is replaced by the projection onto the symmetry axis of the nucleus, Ω. Since the angular distribution depends on Ω, it is also a good idea to divide $g(r)$ into different components corresponding to different Ω. Following the same procedure as in Section 3.1.3, one then arrives at

$$g^{\Omega}_{j\ell}(r) = \sum_N R^*_{N\ell}(r)\int \Phi^*(\mathbf{x}_1,\ldots,\mathbf{x}_A)\Psi(\mathbf{x}_1,\ldots,\mathbf{x}_{A-1})R_{N\ell}(r_A)[Y_\ell(\Omega_A),\chi]_{j\Omega}d\mathbf{x}_1\ldots d\mathbf{x}_A, \tag{4.5}$$

where Φ is the wave function of the mother nucleus, Ψ is the wave function of the daughter nucleus, $R_{N\ell}[Y_\ell,\chi]_{j\Omega}$ are harmonic oscillator wave functions, and j and ℓ are total and orbital angular momenta, respectively, for the proton.

When evaluating this, the neutron part separates from the proton part of the integral. Moreover, the proton wave function is still separate from the daughter nucleus, and is evaluated as a superposition of pure harmonic oscillator particle excitations to the daughter nucleus. Thus,

$$g^{\Omega}_{j\ell}(r) = \langle M_n|D_n\rangle\sum_N R^*_{N\ell}(r)\,\langle M_p|a^{osc\dagger}_{N\ell j\Omega}|D_p\rangle\,, \tag{4.6}$$

where the short-hand notations $|M\rangle$ and $|D\rangle$ are used for the mother and daughter nuclei, respectively, the subscripts n and p indicate whether the neutron states or the proton states are considered, and $a^{osc\dagger}_{N\ell j\Omega}$ is a particle creation operator in the harmonic oscillator orbital $|N\ell j\Omega\rangle$.

In order to evaluate Eq. 4.6, three different components need to be evaluated: the neutron overlap $\langle M_n|D_n\rangle$, the proton overlap $\langle M_p|a^{osc\dagger}_{N\ell j\Omega}|D_p\rangle$, and the radial harmonic oscillator basis functions $R^*_{N\ell}(r)$. These three parts are studied in detail in the following sections.

4.1.3 Nuclear Overlaps

General Treatment

The goal in this section is to compute the overlaps $\langle M_p|a^{osc\dagger}_{N\ell j\Omega}|D_p\rangle$ and $\langle M_n|D_n\rangle$, where mother and daughter nuclei might have different deformations.

First, the potential depth was calculated by using an optimisation algorithm to obtain an energy of 1.53 MeV for the 27th proton. It turned out that $V_0 \sim 50\,\text{MeV}$ for a large range of deformations, and since the exact value of this was not expected to be significant for the results, $V_0 = 50\,\text{MeV}$ was used in further calculations to save time.

The HFB equations Eq. 3.3, were solved in the diagonalised (Hartree-Fock, henceforth HF) basis, in the same way as in Section 3.1.1. Here, one should recall that Ω is a preserved quantum number in this basis (which is assured by the splitting term in the original Hamiltonian), and therefore Eq. 3.6 may be used straightaway for the off-diagonal elements. The Fermi level, λ, was obtained by solving Eq. 3.3 iteratively, and minimising the square of the residual

$$r(\lambda) = (\langle\mathcal{N}(\lambda)\rangle - Z)^2 \tag{4.7}$$

using Newton's method,

$$\lambda_{i+1} = \lambda_i - \frac{r'(\lambda_i)}{r''(\lambda_i)} \approx \lambda_i - \Delta\lambda\frac{r(\lambda+\Delta\lambda) - r(\lambda-\Delta\lambda)}{2(r(\lambda+\Delta\lambda) - 2r(\lambda) + r(\lambda-\Delta\lambda))}, \tag{4.8}$$

where λ_i is the value of λ obtained after each iteration and $\Delta\lambda$ is a small number. The latter expression may be used when no explicit expression for the derivative can be obtained. This method was selected since it has quadratic convergence, while for example Golden Section search only has linear convergence. However, Newton's method is notably unstable, and therefore one should either be careful when picking a starting point λ_0, or modify the method to make it stable. I chose the former option, since it turned out that Newton's method ran smoothly using $\lambda_0 = 1.5\,\text{MeV}$ for the proton states and $\lambda_0 = -7.5\,\text{MeV}$ for the neutron states of ^{52}Fe. When iterating over a large range of deformations, the previous value of λ (i.e., an optimised value at a slightly different deformation) was used as an initial guess. For each deformation, the iteration was terminated when $|\langle\mathcal{N}(\lambda)\rangle - Z| < 0.01$.

The HF basis is, however, not conserved for different deformations. In order to compute overlaps between states with different deformations, one needs to first transform to a common basis. Since the Schrödinger equation is solved in a spherical harmonic oscillator basis, the natural choice is to transform HF states to corresponding harmonic oscillator states.

In the process of diagonalisation, the diagonalised Hamiltonian H^{HF} is obtained as

$$H^{HF} = D^H H^{osc} D, \tag{4.9}$$

where H^{osc} is the oscillator Hamiltonian and D is a matrix consisting of eigenstates. This mapping may be used to transform a vector of annihilation operators a^{HF} to an analogous vector in a harmonic oscillator basis, which is done through

$$a^{osc} = Da^{HF}. \tag{4.10}$$

Using the matrix representation of Eq. 3.27, U is then transformed from HF to oscillator basis through

$$U^{osc} = DU^{HF}, \tag{4.11}$$

where the superscripts denote which bases are used, and analogous for V. In order to satisfy the symmetry requirements for U and V (given in [9, p. 615]) in a harmonic oscillator basis, it is important that the relative phase between two eigenvectors corresponding to states of the same energy but opposite spins is zero. This was ensured by adjusting the phase factors (which are arbitrary) of the column vectors in D.

One should note that the basis states become permuted when solving the HFB equations, i.e., U and V are not diagonal. This may be resolved by permuting U and V to a diagonal matrix (in the non-degenerate case, these consist of pure HF states), which was necessary to keep track of the quantum numbers belonging to each vector U_k.

Proton Overlap

The proton overlap $\langle M_p|a^{osc\dagger}_{N\ell j\Omega}|D_p\rangle$ was computed as in the work preceding Eq. 3.38, except that $U, V, \tilde{U}$, and $\tilde{V}$ are now computed in a harmonic oscillator basis (this is required both for obtaining a common basis, and to create the emitted proton in a pure harmonic oscillator orbital), yielding the result

$$\langle M_p|a^{osc\dagger}_{N\ell j\Omega}|D_p\rangle = \langle \tilde{D}_p|D_p\rangle \left(\tilde{U}^*_{N\ell j\Omega,k} - \left(\tilde{V} \left(U^H\tilde{U} + V^H\tilde{V} \right)^{-1} \left(V^H\tilde{U}^* + U^H\tilde{V}^* \right) \right)_{N\ell j\Omega,k} \right). \tag{4.12}$$

In this model, the projection onto the interesting ℓ, j state is obtained by finding the (perhaps small) components of the original emitted proton state, which have these quantum numbers.

The overlap $\langle \tilde{D}_p|D_p\rangle$ was computed by using the Onishi formula Eq. 3.39, again using an harmonic oscillator basis. For this evaluation, 13 harmonic oscillator shells were used.

In order to get the correct quasiparticle excitation for the mother nucleus, one should be careful to pick a pure Ω state, since this quantum number is the only one – except for parity – which is preserved in the deformed case. It is required that $\Omega = 7/2$ for the single proton in ^{53}Co, in order to couple to a total angular momentum $I = 19/2$ when including neutrons. This puts the state at maximum projection onto the symmetry axis, which is required to obtain approximately correct angular momentum, since j is no longer a good quantum number. In this way, one only needs to evaluate Eq. 4.12 for $\Omega = 7/2$. This was solved by comparing Ω values of the dominant component of each eigenstate to the Hamilton operator, and picking the lowest energy level with $\Omega = 7/2$ as state k, since no state with lower energy has this value of Ω.

Neutron Overlap

In order to obtain a nuclear angular momentum of $I = 19/2$, it is required that the neutrons couple to $J = 6$. This requires that a neutron pair breaks up and the two neutrons are put in different orbitals, with $\Omega = 7/2$ and $\Omega = 5/2$, respectively. Practically, this is achieved by moving one of the neutrons in an $\Omega = \pm 5/2$ subshell, which is fully occupied in the ground state, to one of the empty $\Omega = \pm 7/2$ subshells. Due to pairing, all of these shells are mixtures between particle and hole states. Consequently, the breaking of pairs is achieved by adding two quasiparticles to the ground state, one at $\Omega = 7/2$ and one at $\Omega = 5/2$. Denoting the

corresponding quasiparticle creation operators by $\tilde{\beta}_1^\dagger$ and $\tilde{\beta}_2^\dagger$, I therefore want to compute the overlap

$$\langle D_n|\tilde{\beta}_1^\dagger\tilde{\beta}_2^\dagger|\tilde{D}_n\rangle\,,$$

where it should be emphasised that the quasiparticles are created on the $\tilde{D}$ state. Using the definition Eq. 3.27 for the quasiparticle creation operator and the relations Eq. 3.36–3.37, one arrives after some simplification at

$$\begin{aligned}\langle D_n|\tilde{\beta}_1^\dagger\tilde{\beta}_2^\dagger|\tilde{D}_n\rangle = \langle D_n|\tilde{D}_n\rangle \Big(&-\tilde{U}_2^T(V(\tilde{U}^H U+\tilde{V}^H V)^{-1}\tilde{U}^H)\tilde{U}_1+\tilde{U}_1^T(V(\tilde{U}^H U+\tilde{V}^H V)^{-1}\tilde{V}^H)\tilde{V}_2\\ &+\tilde{U}_2^T(\mathbf{1}-V(\tilde{U}^H U+\tilde{V}^H V)^{-1}\tilde{V}^H)\tilde{V}_1+\tilde{V}_1^T(U(\tilde{U}^H U+\tilde{V}^H V)^{-1}\tilde{V}^H)\tilde{V}_2\Big)\,,\end{aligned} \tag{4.13}$$

where $\tilde{U}_1$ is the hole occupancy vector corresponding to $\tilde{\beta}_1$ and analogous for $\tilde{U}_2$, $\tilde{V}_1$ and $\tilde{V}_2$.

When solving the Schrödinger and HFB equations for neutrons, the same procedure as for protons was applied, except that the Coulomb potential was removed and the search for the correct quasiparticle states also put a requirement on j in order to excite an $f_{7/2}$ state with $\Omega = 5/2$, and not a $d_{5/2}$ state, which would had otherwise been the case. Otherwise, putting a requirement on parity would have had the same effect.

Nilsson Diagrams

As a first validation of the diagonalisation procedure, energy levels were plotted against deformation for both proton and neutron levels – i.e., Nilsson diagrams were constructed – for ^{52}Fe. This was done by connecting states with the same Ω quantum numbers and parity, in a way that levels with these quantum numbers did not cross.

4.1.4 Connecting Overlaps to Radial Basis Functions

In order to evaluate the half-life, all the pieces in Eq. 4.6 were put together, i.e., the non-zero overlap coefficients computed in Section 4.1.3 were multiplied with appropriate radial harmonic oscillator basis functions.

The latter are obtained as [6, p. 79]

$$R_{N\ell}(\rho) = C\rho^\ell F\left(-n, \ell+\frac{3}{2}, \rho^2\right)\exp(-\rho^2/2), \tag{4.14}$$

where

$$\rho = \sqrt{\frac{M\omega_0}{\hbar}}\cdot r, \tag{4.15}$$

with definitions as in Section 2.1.6. Here, F is Kummer's function Eq. 2.17, n is the radial quantum number, defined in Eq. 2.50, and C is a normalisation constant. When using a negative integer number $-n$ as the first argument of Kummer's function, the sum in Eq. 2.17 terminates at $k = n$ steps. Thus, only a few terms of Kummer's function need to be evaluated. The oscillator frequency ω_0 was evaluated using Eq. 2.48.

Here, the idea is to use the approach in Section 2.1.3 to calculate the half-life. This is done by matching the internal wave function to an external one, by using Eq. 2.27. The external wave function is approximated as a Coulomb wave function Eq. 2.25 with $\ell = 9$. This is actually only valid in spherical symmetry, but since the deformations of the nuclei involved here are not very large, this was expected to be a reasonable approximation. Since both the internal wave function and the external one have angular distributions $\propto Y_{\ell\Omega}(\theta,\phi)$,

one should be able to match these. Then one can use Eq. 2.27 directly to find the decay constant, and consequently the half-life.

For ^{53}Co, where $\ell = 9$ and $j = 19/2$, 13 oscillator shells were used to evaluate Eq. 4.6. This was done to get non-zero coefficients for as many radial basis functions as possible (three) within a reasonable computation time. Then, the possible basis functions are $R_{9,9}$, $R_{11,9}$, and $R_{13,9}$.

The resulting projections were matched to an appropriate Coulomb wave function Eq. 2.25 with parameters corresponding to $l = 9$ and $Q = 1.53\,\text{MeV}$. Since the position of the potential barrier was unknown, matching points were selected on quite a wide interval, $r \in [5, 20]\,\text{fm}$.

4.2 Results

A Nilsson diagram for the proton states in ^{52}Fe is shown in Figure 4.1. A Nilsson diagram for neutrons was also constructed, but since this is very similar and there are not any unexpected features, this is not included in this report. The levels are colour-coded to distinguish between energy levels corresponding to different Ω and parity. Comparing this figure to Figure 2.21a in [9, p. 73], shows a strong agreement for bound states (negative energy).

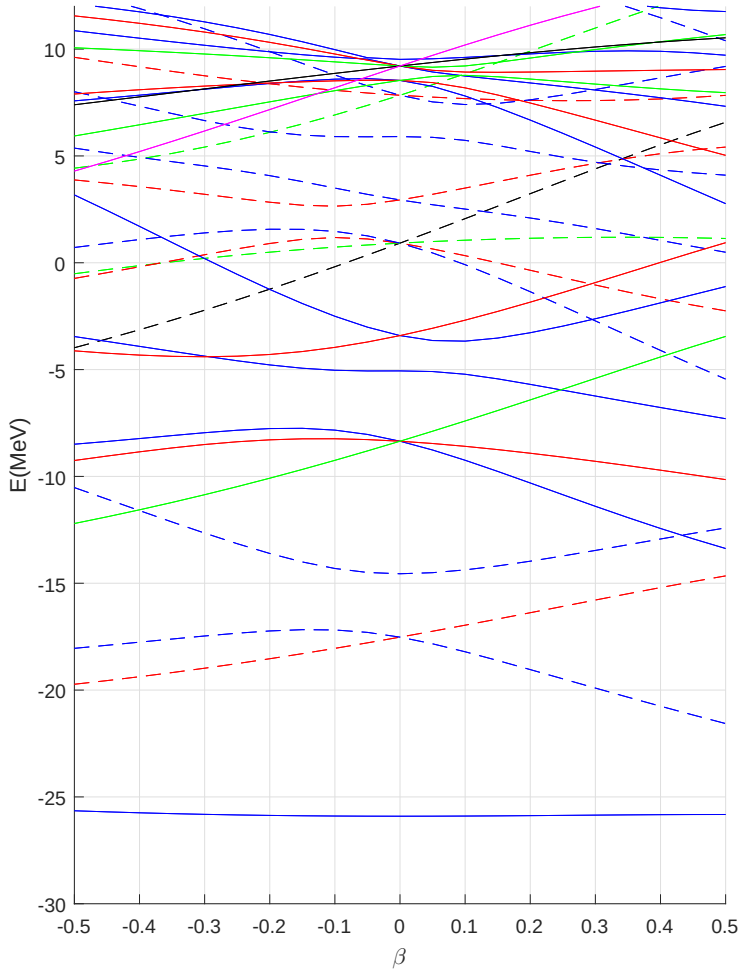

Figure 4.1 – Nilsson diagram for the proton states of ^{52}Fe. Solid lines correspond to even parity and dashed lines correspond to odd parity. Colour coding: blue – $\Omega = \pm 1/2$, red – $\Omega = \pm 3/2$, green – $\Omega = \pm 5/2$, black – $\Omega = \pm 7/2$, magenta – $\Omega = \pm 9/2$.

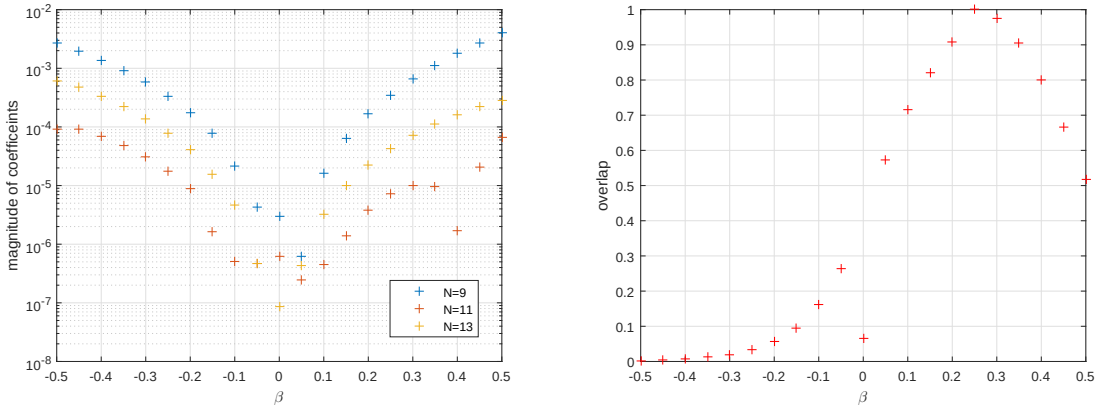

(a) **(b)**

Figure 4.2 – **(a)** Coefficients in front of the three radial basis functions R_{N9}, $N = 9, 11, 13$, as defined by Eq. 4.16, as a function of β_2 (denoted β) of the mother nucleus, for decay of ^{53}Co. For the daughter nucleus, $\beta_2 = 0.25$. Note the logarithmic scale. **(b)** Overlaps between proton orbitals $\langle \tilde{D}_p | D_p \rangle$ for ground states with different deformations, computed for ^{52}Fe using 13 oscillator shells. Here, $\beta_2 = 0.25$ for $|D_p\rangle$ and the overlaps are computed as a function of β_2 for $|\tilde{D}_p\rangle$.

Coefficients

$$\tilde{U}^*_{N\ell j\Omega,k} - \left(\tilde{V} \left(U^H \tilde{U} + V^H \tilde{V} \right)^{-1} \left(V^H \tilde{U}^* + U^H \tilde{V}^* \right) \right)_{N\ell j\Omega,k} \tag{4.16}$$

corresponding to oscillator basis functions with $l = 9$, are plotted for ^{53}Co for different deformations in Figure 4.2a. It appears that the $N = 9$ component is typically about one order of magnitude greater than the $N = 13$ component, and another order of magnitude greater than the $N = 11$ component. Moreover, the coefficients are all very small at near-spherical shapes, and their magnitudes increase with deformation.

Proton overlaps $\langle \tilde{D}_p | D_p \rangle$, where $\beta_2 = 0.25$ for the daughter nucleus, are shown for different deformations of the mother nucleus in Figure 4.2b. This dependence appears to be near-Gaussian, except when $\beta_2 = 0$, where the overlap is more suppressed.

The effects described above are summarised in Table 4.1, computed for $\beta_2 = 0.10$ and $\beta_2 = 0.15$, respectively, for the mother nucleus.

The neutron overlap between a mother nucleus with quasiparticle excitations in the $\Omega = 7/2$ and $\Omega = 5/2$ orbitals, and the daughter nucleus, becomes zero when using the treatment in Section 4.1.3, regardless of deformation of the mother nucleus and the number of oscillator shells used. This indicates that another method or model is required to explain and compute this overlap.

Table 4.1 – Change in decay probability due to different effects, computed for $\beta_2 = 0.10$ and $\beta_2 = 0.15$, respectively, for the mother nucleus ^{53}Co, whereas $\beta_2 = 0.25$ is used for the daughter nucleus. In all of these computations, 13 oscillator shells are used. The $R_{9,9}$ component is displayed here, since this is the largest one.

Quantity	$\beta_2 = 0.10$	$\beta_2 = 0.15$
Square of coefficient in front of $R_{9,9}$	$2.7 \cdot 10^{-10}$	$4.0 \cdot 10^{-9}$
$\lvert \langle \tilde{D}_p \lvert D_p \rangle \rvert^2$	0.51	0.67

Projected probability amplitudes $|g(r) \cdot r|$, as defined in Eq. 4.6, constructed using the three

calculated components in Figure 4.2a are shown for deformations $\beta_2 = 0.1$ and $\beta_2 = 0.15$ in Figure 4.3a. Here, the neutron overlap has been set to one, due to the problems with obtaining this. There are not any large differences in shape of $|g(r)|$ between the two deformations, although the amplitude varies by about a factor of three. In both cases, there is a sharp node in the wave function at $r \approx 10\,\mathrm{fm}$.

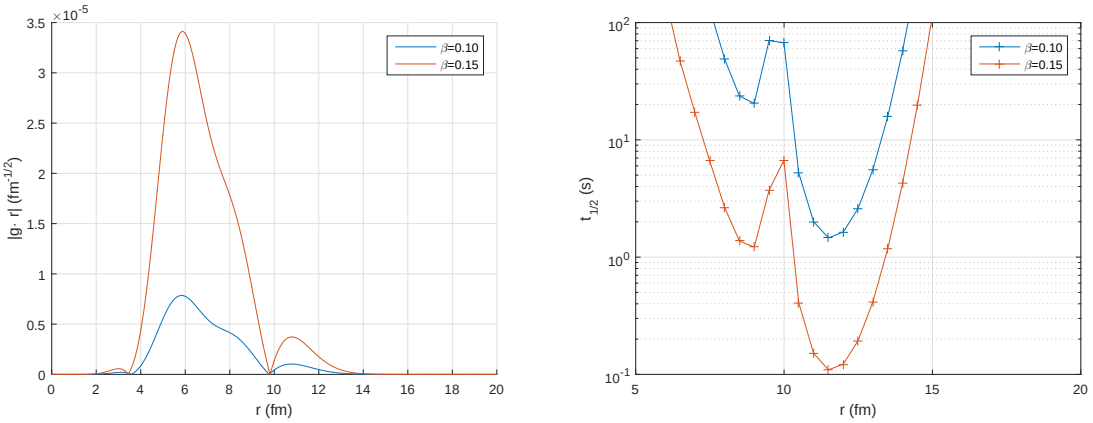

(a) **(b)**

Figure 4.3 – **(a)** Projected probability amplitudes $|g_{j\ell}(r)\cdot r|$ – defined in Eq. 4.6 – as a function of distance from the core in ^{53}Co, computed using 13 oscillator shells for deformations $\beta = 0.10, 0.15$, for $\ell = 9$ and $j = 19/2$ for an emitted $f_{7/2}$ proton. Here, the effect of the neutron overlap has been excluded. **(b)** Corresponding half-lives computed at matching points marked by '+' using the method described in Section 4.1.2. Note that the scale is logarithmic. The plot has been cut in order to avoid including extremely long decay times.

Resulting half-lives obtained using the method described in Section 4.1.2, computed at different matching points, cf. Eq. 2.26, on the interval $r \in [5, 20]\,\mathrm{fm}$, are given in Figure 4.3b. The results vary very much over the interval, contrary to the analogous calculations in spherical symmetry (cf. Figure 2.2). Therefore, the minimum values for each deformation are given in Table 4.2, to put a lower bound on the half-life obtained from this method. Here, the trend is opposite from the probability amplitude, which can be seen directly from Eq. 2.27 and Eq. 2.31. These values of $t_{1/2}$ are about 1-2 orders of magnitude lower than the experimental estimate.

Table 4.2 – Minimum values of the ^{53}Co half-lives given in Figure 4.3b, computed for each deformation β_2.

β_2	Minimum $t_{1/2}$ (s)
0.10	1.5
0.15	0.11

4.3 Discussion

When constructing Nilsson diagrams (Figure 4.1) for illustrating migration of energy levels under deformation, the development for bound states is very similar to when using a modified harmonic oscillator potential [9, p. 73]. For quasibound states, the spectrum is again denser than in the harmonic oscillator case, which is consistent with the discussion for the level spectrum in the spherical case. This validates the computations used in Section 4.1.

The dependence on deformation for the overlap between proton states (cf. Figure 4.2b) appeared to follow a near-Gaussian distribution, which is consistent with the Gaussian Overlap Approximation [9, pp. 424-428]. However, the significantly smaller overlap between a nucleus with $\beta_2 = 0.25$ and one with $\beta_2 = 0$, deviates from this. A possible explanation is that numerical errors arise due to the large degeneracies present for spherical nuclei, and that these are not completely resolved by the infinitesimal splitting term. This was, however, not investigated further.

The magnitudes of the harmonic oscillator components with $\ell = 9$ increase with deformation. This is quite an expected effect, since the mixing between components of different ℓ increases with deformation. For spherical nuclei, ℓ is expected to be a pure quantum number, and therefore components of $\ell = 9$ should not be present in the proton wave function. However, since components of the daughter wave function enter the projection formula (cf. Eq. 4.12), there are components with larger values of ℓ in the emitted proton wave function as well.

Since the deformation difference between the mother and daughter nuclei is not very large ($\Delta\beta_2 \sim 0.10-0.15$), the overlap between proton states is quite large. Therefore, the structural changes of the proton orbitals are not a significant hindrance factor for the decay time.

When obtaining a zero overlap between the neutron states, one might think that there is an error somewhere, since the proton decay of ^{53}Co obviously has been observed. However, in order for this overlap to be non-zero, there need to be mixings between the $\Omega = 5/2$ and the $\Omega = 7/2$ states in the mother nucleus. For axially symmetric nuclei, though, Ω is preserved, and therefore these states cannot mix, meaning that a different model is required to explain this overlap.

Here, two different explanations are possible. Either the mother nucleus is triaxial, since Ω is not a good quantum number in triaxial nuclei, or there exist significant interactions between the protons and neutrons in the daughter nucleus. As suggested by [14], particularly strong mixings between protons and neutrons might exist in $N = Z$ nuclei, making this a possible explanation. In this case, there might exist a component in the wave function of the daughter nucleus, where the neutrons couple to $I = 6$, which is counteracted by protons coupled to $I = 6$, anti-parallel to the neutrons. In this model, the proton would leave from the $\Omega = 5/2$ orbital and no structural change of the neutrons is required. However, since the proton and neutron angular momenta have parallel coupling, this would require flipping of the proton angular momentum, disfavouring this hypothesis.

In the final calculation, the obtained half-life was $\sim 0.1 - 1\,\mathrm{s}$, or about 1-2 orders of magnitude smaller than the experimental estimate. If all other calculations are correct, this should therefore be the magnitude of suppression caused by the neutron overlap. Before drawing any conclusions, however, the approach used in Section 4.1.2 should be validated, and in particular the matching procedure, especially since Coulomb wave functions assume spherical symmetry. There was unfortunately not time to do this during the work of this thesis, but a few things may be discussed. In particular, it is expected that the computed half-life should be constant in the potential barrier and further out, which is certainly not the case here (cf. Figure 4.3b). This should be resolved by including more oscillator shells, since only using three components does not give an accurate behaviour far from the core. However, this would significantly increase the computation time, and it was beyond the scope of this thesis to optimise the code enough to be able to carry out these computations using enough oscillator shells. Therefore, the minimum value was printed, since the position of this was expected to be somewhere in the potential barrier.

As a validation of the method, one may look at the coefficients in front of $R_{N\ell}$ directly and apply these to the extrapolated value of $t_{1/2} \sim 5 \cdot 10^{-10}$ s in the spherical case (cf. Section

2.2.3). Since these factors (including the proton overlap) give a suppression of $\sim 4 \cdot 10^8 - 7 \cdot 10^9$ (cf. Table 4.1), the resulting value of $t_{1/2} \sim 0.2 - 4\,\mathrm{s}$, or about a factor of two greater than the results in Table 4.2. This implies that the results – within this model – are within the correct order of magnitude.

In order to accurately determine the half-life, one should in addition to the work done in this thesis, include overlap effects between the emitted proton and the daughter nucleus, i.e., leave the assumption that the daughter nucleus and the proton may be treated as separate particles. Such effects are expected to be quite small, but since the magnitudes of the components with $\ell = 9$ also are quite small, these effects may have significant effects on the results. Moreover, a more accurate model should be used for the matching procedure.

With the then obtained half-life, the new measurement of the partial half-life of ^{53}Co in the proton channel may be used to determine the magnitude of the neutron overlap. This may be fit to the common parametrisation γ for the triaxial shape of the mother nucleus, cf. [6, pp. 126-131]. Possible values of γ may then be tested by checking if it is reasonable that some of these minimise the energy of ^{53}Co. If not, more exotic explanations of the neutron overlap should be considered, such as p-n interactions.

These final suggestions are a natural extension of this thesis. If being successful in explaining the decay of ^{53}Co, the new measurement may furthermore be used to refine model parameters. This would also open up possibilities to study other complex, neutron deficient nuclei.

Chapter 5

Conclusions

The methods WKB, TPA and PFA all produce accurate results for spherical nuclei without structural changes, which validates that PFA is a useful method for studying proton emission. Moreover, PFA may be extended beyond the spherically symmetric situation, and be used for studying deformed nuclei where structural changes occur.

If not taking into account any structural changes and falsely assuming that $\ell = 3$ for the emitted proton in ^{53}Co, the computed half-life is about 17 orders of magnitude lower than an experimental estimate. The relevant factors for describing this suppression are the increase in angular momentum to $\ell = 9$ (adds an estimated factor of $\sim 3 \cdot 10^6$), and the magnitude of the components of the proton wave function with $\ell = 9$ (adds a factor of $\sim 4 \cdot 10^8 - 7 \cdot 10^9$), and the transformation of neutron orbitals. On the other hand, the overlap between proton orbitals, and differences in pairing gap between mother and daughter nuclei, are not significant effects for explaining the suppression in decay probability.

With the assumptions used in this thesis, it was not possible to compute the overlap between neutron orbitals. This should be resolved by extending this work to triaxial shapes, and using the new measurement to estimate model parameters. If this is not successful, more exotic explanations might be considered.

Bibliography

[1] Åberg, S., Semmes, P., Nazarewicz, W. *Phys. Rev. C 56:4 (1997): 1762-1773.* Spherical proton emitters.

[2] Vertse, T., Pál, K.F., Balogh, Z. *Com. Phys. Commun. 27 (1982): 309-322.* Gamow, a Program for Calculating the Resonant State Solution of the Radial Schrödinger Equation in an Arbitrary Optical Potential.

[3] *Chart of Nuclides.* Brookhaven National Laboratory, National Nuclear Data Center. Electronic source, retrieved on July 8, 2015. http://www.nndc.bnl.gov/chart/

[4] Jackson, K.P. et al. *Phys. Lett. 33B: No. 4 (1970): 281-283.* ^{53m}Co: A Proton-Unstable Isomer.

[5] Sarmiento, L.G. *Nuclear spectroscopy with Geant4: Proton Radioactivity.* (2015). Talk given at the 13th Nordic Meeting on Nuclear Physics, Saariselkä, Finland.

[6] Nilsson, S.G., Ragnarsson, I. *Shapes and Shells in Nuclear Structure.* (1995). Cambridge University Press, Cambridge, UK.

[7] Abramowitz, M., Stegun, I.A. *Handbook of Mathematical Functions with Formulas, Graphs, and Mathematical Tables (Partially Mathcad-enabled).* (1972). U.S. Department of Commerce, NIST.

[8] Mang, H.J. *Annual Review of Nuclear Science 14 (1964): 1-26.* Alpha Decay.

[9] Ring, P., Schuck, P. *The Nuclear Many-Body Problem.* (1980). Springer-Verlag, Berlin Heidelberg, Germany.

[10] Bengtsson, R., Garrett, J.D. *International Review of Nuclear Physics - Vol.2 1984. Collective Phenomena in Atomic Nuclei, 194-336.* The Cranking Model - Theoretical and Experimental Bases. World Scientific Co., Singapore.

[11] Hasse, R.W., Myers, W.D. *Geometrical Relationships of Macroscopic Nuclear Physics.* (1988). Springer-Verlag, Berlin Heidelberg, Germany.

[12] Hilaire, S., Girod, M. *Hartree-Fock-Bogoliubov Results Based on the Gogny Force.* CEA, France. Electronic source, retrieved on December 15, 2015. http://www-phynu.cea.fr/science_en_ligne/carte_potentiels_microscopiques/carte_potentiel_nucleaire_eng.htm

[13] Ingemar Ragnarsson. Private communication.

[14] Cederwall, et al. *Nature 469 (2011): 68-71.* Evidence for a spin-aligned neutron–proton paired phase from the level structure of ^{92}Pd.